UNIVERSITY OF SOUTHAMPTON

DEFECTS IN EPITAXIAL II-VI SEMICONDUCTORS

Adam Wasenczuk M.A. (Cantab.)

Doctor of Philosophy

Department of Engineering Materials

September 1998

UNIVERSITY OF SOUTHAMPTON

ABSTRACT

FACULTY OF AERONAUTICAL AND ASTRONAUTICAL ENGINEERING

ENGINEERING MATERIALS

Doctor of Philosophy

DEFECTS IN EPITAXIAL II-VI SEMICONDUCTORS

by Adam Wasenczuk

II-VI compounds find application in infra-red detectors, solid-state lasers and other optical devices. They are frequently produced as epitaxial layers on substrates of other materials. Crystalline defects in the layers affect their properties. Many defects in II-VI epitaxial layers are produced unintentionally during growth by 'relaxation'. Understanding of relaxation is necessary for control of material properties.

In this work, new techniques have been developed for the successful direct observation of defects in cadmium telluride and cadmium mercury telluride epitaxial layers by transmission electron microscopy in both plan-view and cross-section, and this has allowed the relaxation mechanisms to be elucidated. The study has included liquid-phase epitaxial and metal-organic vapour-phase epitaxial material. Surface topography of layers has been observed in detail with atomic force microscopy, to understand the effect of chemistry on growth, and attempts have been made to correlate surface features with crystalline defects.

A previously unobserved ordered second phase has been observed in CMT layers on GaAs, and characterised.

CONTENTS

1\. **INTRODUCTION**

2\. **LITERATURE**

3. **EXPERIMENTAL**

4. **RESULTS**

5. DISCUSSION

6. CONCLUSION & FUTURE WORK

7. REFERENCES

1. INTRODUCTION

II-VI compounds (pronounced 'two six') have become commercially important in electronic applications such as infra-red detectors, solid-state lasers and other optical devices. Increasingly, the materials are being deposited as 'epitaxial' layers on other substrates because a higher degree of crystalline perfection and compositional control can be achieved.

Crystalline perfection is necessary for good electronic properties in these materials, because they are semiconductors. Increased compositional control is needed for the production of more advanced devices. Though a higher degree of crystalline perfection can be achieved in an epitaxial layer, there remains much room for improvement. This project was therefore intended to investigate in detail the reasons for the absence of crystalline perfection in these materials.

The initial aim of this work was to examine diffusional phenomena in II-VI compounds. This was because diffusional doping can be used in the production of II-VI devices.

A literature review suggested that diffusion was also a matter of academic interest. Disagreements were found in many areas. These disagreements suggested to the present author that some research groups were not controlling the variables in their experiments sufficiently. The conclusion drawn from the literature survey was that the uncontrolled variable was microstructure.

Therefore, it became the opinion of the present author that before any diffusion experiment could be performed on a specimen, its microstructure had to be known. That is, the results of a diffusion experiment should be interpreted in terms of the microstructure of the specimen.

It was also found that the microstructure of an epitaxial layer of material should be affected by the phenomenon of 'relaxation'. Therefore, it became the opinion of the present author that the results of any microstructural examination of an epitaxial later should be interpreted in terms of relaxation theory.

The remainder of this work therefore describes investigations of the microstructure of various II-VI epitaxial layers, and attempts to explain the ways in which the observed features were formed. Novel techniques have been developed by the present author to this end, and previously unobserved features have been identified and interpreted.

2. LITERATURE

Cadmium telluride and cadmium mercury telluride ('CMT') are two commercially important II-VI compounds. Tellurium is a group VI element, and cadmium and mercury, being 'd'-block elements in the periodic table, are commonly termed 'group II' in semiconductor literature. Cadmium mercury telluride contains approximately equal numbers of (partially ionised) d-block atoms and tellurium atoms, but the ratio of the cadmium and mercury concentrations is freely variable. The material is commonly given the formulae $Cd_xHg_{1-x}Te$ or (Cd,Hg)Te. Thus CdTe is a special case of CMT. For many values of x, the material is a semiconductor; the band-gap increases monotonically with x from zero at $x = 0.16$.

2.1 Structure of Cadmium Mercury Telluride

The structure of perfect crystals of cadmium mercury telluride is described in the following section. However, the perfect structure of any crystal is stable only at absolute zero. This is because a structure is stable only when it has minimum free energy, and free energy contains an entropy term. That is, a small concentration of defects is statistically likely in every crystal, despite the fact that defects take energy to form, because every crystal has some thermal energy. In this section, the structure of CMT and the possible defects associated with it will be discussed.

2.1.1 Crystal Structure of CMT

Cadmium Mercury Telluride (CMT) has the 'zinc-blende' or 'sphalerite' structure. This is face-centred cubic, with the motif:

Cd or Hg: (0, 0, 0)
Te: ($\frac{1}{4}$, $\frac{1}{4}$, $\frac{1}{4}$)

i.e., two interpenetrating 'sub'-lattices.

The Cd and Hg atoms could either be randomly distributed among sites, or ordered. In the random arrangement, the ratio of Cd to Hg concentration determines the band-gap of the material, as discussed above. Material of graded composition has graded band-gap.

The (111) stacking sequence in a close-packed cubic (CCP) material is written '...ABCABC...'. In CMT, because of the motif, the stacking sequence is:

$$\ldots\ \mathrm{Hg}_A\ \mathrm{Te}_A\ \mathrm{Hg}_B\ \mathrm{Te}_B\ \mathrm{Hg}_C\ \mathrm{Te}_C\ \ldots$$

where 'A', 'B' and 'C' are the stacking sites. However, another distinct stacking sequence is possible:

$$\ldots\ \mathrm{Te}_A\ \mathrm{Hg}_A\ \mathrm{Te}_B\ \mathrm{Hg}_B\ \mathrm{Te}_C\ \mathrm{Hg}_C\ \ldots$$

This indicates that the structure is not centrosymmetric. A non-centrosymmetric crystal may not easily be oriented by X-ray diffraction. This is because any crystal with a real structure factor must produce a centrosymmetric diffraction pattern. Crystals of CMT may, however, be oriented by X-ray diffractography if the X-ray wavelength is chosen such that the phase of the radiation is shifted upon its interaction with one of the types of atom in the material. Phase shifts can be represented by complex structure factors, and crystals with complex structure factors may give rise to non-centrosymmetric diffraction patterns (Fewster et al. (1981)).

2.1.2 Point Defects

The conventional notation for point defects (Kröger 1974), with reference to the system under consideration, is as follows. Each species has a name, and a site in subscript (as above for the description of stacking sequence). A vacancy is given symbol 'V'. An interstitial site is 'i'. Where Cd and Hg are randomly distributed across their sites, all these 'metal' sites are equivalent and are given the site symbol 'M'. Thus a metal vacancy has the symbol V_M. If dislocation climb is allowed, vacancy pairs may be freely created or destroyed. This reaction may be written:

$$V_M + V_{Te} = 0 \quad \ldots(2.1)$$

Charges are indicated by superscript: negative by "'" and positive by '·'.

Intersitials and vacancies all diffuse; obviously the phenomena can be complex in a three-component system. However, in most references it is agreed that antisite defects can be neglected in an accurate description of the system.

2.1.3 Dislocations

Dislocations in CMT lie on (111) planes, as is usual in a close-packed cubic (CCP) structure. Two distinct types of dislocation can exist in CMT: between planes with the same stacking site (A, B or C), and between planes of different stacking sites. These are termed 'shuffle' and 'glide' respectively, in all the references discussed below. The 'glide' dislocations are thought to be similar in structure to dislocations in CCP metals, and are therefore thought to exist as paired partials separated by a stacking fault.

Because dislocations lie between planes of unlike atoms, positive and negative dislocations have different core structures. The convention for this is as follows:

1. Consider an octahedral crystal with (111) faces.
2. Let these faces terminate in triply-bonded atoms.

3. Then four faces terminate in metal atoms; the other four terminate in tellurium atoms.
4. (111) is a metal face.

It is obvious to the present author that:

1. A positive dislocation on (111) is identical to a negative dislocation on $(\underline{111})$.
2. Dislocation climb requires the motion of both species.
3. A shuffle dislocation can climb into a glide dislocation and vice-versa by the motion of only one species.

Osip'yan et al. (1986) reviewed experiments in which, the mobile dislocation set (shuffle or glide) being known, the mobilities of the two types of dislocation (M or Te) could be compared. Barbot et al. (1988) performed an experiment in CMT and concluded that Te glide dislocations were dominant.

2.1.4 Twins

A twin is formed when the stacking sequence in a material reverses. For example, consider the (111) stacking sequence above, with the introduction of a twin boundary:

$$\ldots\ Hg_A\ Te_A\ Hg_B\ Te_B\ Hg_C\ Te_C\ Hg_B\ Te_B\ Hg_A\ Te_A\ \ldots$$

Because of the compound nature of the material, the twin cannot be described by a reflection in the (111) plane. That would create an antiphase boundary. This is instead a 'rotation' twin: the twin is formed by rotating the planes on one side of the twin boundary by 180° about the twin plane normal.

Let the coordinate axes be orthogonal. For a rotation of 180° about [111]:

(100) maps to $\frac{1}{3}(\underline{1}22)$
(010) maps to $\frac{1}{3}(2\underline{1}2)$
(001) maps to $\frac{1}{3}(22\underline{1})$.

One can express this transformation by a 3x3 matrix:

i.e., $$\frac{1}{3}\begin{pmatrix}\underline{1}22\\2\underline{1}2\\22\underline{1}\end{pmatrix}\begin{pmatrix}1\\0\\0\end{pmatrix} = \frac{1}{3}(\underline{1}22) \quad \text{etc.,} \quad \ldots(2.2)$$

and similarly for all other directions. Thus the present author chooses to find equivalent directions in the matrix and twin.

2.1.5 Hexagonal and Tetragonal CdTe

In this section is discussed evidence for regions of hexagonal stacking within thin films of CdTe. The density of lattice points in the hexagonal structure is half that of the cubic structure, because a common environment is shared only by atoms in alternate (111) planes. Thus the primitive unit cell of the hexagonal structure is larger than that of the cubic structure; thus the diffraction pattern of the hexagonal structure can contain extra maxima.

The most obvious of these extra maxima would be (0001), indexed in the cubic system as $(\frac{1}{2}\frac{1}{2}\frac{1}{2})$. By inspection, however, this reflection is absent in a random solid solution of CMT. However, Figure 2.1 illustrates that the (111) diffraction patterns of the two structures would differ in scale. Abdalla and Holt (1973) have observed the hexagonal phase, but in a later paper (1974) the matter of scale is not made clear. Pawlewicz (1977) and Spinulescu-Carnaru (1966) have observed the phase in powder diffractography, but this could be due to a very high stacking fault density introduced by pulverisation.

Figure 2.1: The (111) electron diffraction pattern of CMT. Dots indicate diffraction maxima. Those in parentheses () are present only in the hexagonal phase.

Das et al. (1987) claimed to have observed a tetragonal phase of CdTe. The published diffraction pattern is, however, indistinguishable from that of cubic CdTe with [114] incident beam. The authors claimed [110] illumination, but [110] is mapped onto [114] by the twin rotation about [111] discussed above, so it seems possible to the present author that they were observing a twin.

2.1.6 Ordered Phases in CMT

Chang and Goo (1992) have examined $Cd_{0.4}Hg_{0.6}Te$ and have observed an ordered structure of composition $CdHgTe_2$, with four symmetrically related variants in which (111) cationic layers were alternately Cd and Hg. This material would give rise to x-ray or electron diffraction maxima which would be indexed as (½½½) in the cubic system.

Barbot et al. (1988) observed a peak in the hardness of $Cd_xHg_{1-x}Te$ at $x=0.75$, a typical composition for an ordered phase, but could find no other evidence for ordering.

2.1.7 Heterointerfaces

Every epitaxial layer has an interface with its substrate, at which the two are chemically bonded. If the composition of the material changes at this interface, it is referred to as a 'heterointerface'. In general, the physical properties of a material, for example lattice parameter and thermal expansion coefficient, change when the composition is changed. In the present work, CdTe has been deposited epitaxially on GaAs. The lattice parameters of isolated CdTe and GaAs crystals are about 6.5A and 5.6A respectively. The percentage difference between the lattice parameters of the two phases across their interface is called the 'misfit'. Here it is about 14%. A single perfect crystal with one half of composition GaAs and the other of composition CdTe would therefore seem energetically unfavourable, as each half would have about 7% strain. However, the CMT in this work has been deposited on either CdTe (deposited on GaAs) or (Cd, Zn)Te. The misfit between CMT and these materials is much less than that between CdTe and GaAs. The behaviour of both these systems will be discussed in section 2.4.

2.2 Interactions Between Defects in CMT

All the defects in a crystal can interact via diffusion. For example, dislocations can climb by diffusion. Diffusion is commercially important because defects can have electronic effects, and so defects can be introduced by diffusion to create devices. There are several forms of defect interactions reported in the literature, as follows.

2.2.1 Vacancies and p-type Doping

Vydyanath (1981) suggested that 'mercury vacancies' (that is, metal-site vacancies) could behave as doubly ionised acceptors, and that they could be formed by the loss of mercury from the surface to the vapour phase, or vice-versa. If 'h' is a hole, one could have:

$$Hg_M = V_M'' + 2h^{\cdot} + Hg_{(g)} \quad \ldots(2.3)$$

The hole, occupying a band, has no site.

If one approximates that $[Hg_M]$ is constant, then in an atmosphere of Hg partial pressure p_{Hg},

$$[V_M''][h^{\cdot}]^2 p_{Hg} \text{ is constant.} \quad \ldots(2.4)$$

When the material is extrinsically doped by these intrinsic defects (at low temperature):

$$[h^{\cdot}] = 2[V_M]; \quad \ldots(2.5)$$

$$4[V_M]^3 p_{Hg} = \text{constant}. \quad ...(2.6)$$

When the material is intrinsically doped by thermal excitation from valence band to conduction band (room temperature), $[h^{\cdot}]$ is constant and

$$[V_M] p_{Hg} = \text{constant}. \quad ...(2.7)$$

So, Vydyanath annealed CMT in mercury vapour at various temperatures to change the vacancy concentration, then quenched the samples to the extrinsic doping temperature region and measured the hole concentration by the measurement of Hall coefficients. The observations were as expected from the above equations.

2.2.2 n-type Doping

2.2.2.1 By Point Defects

Jones et al. (1982) proposed that if mercury vacancies were acceptors, mercury interstitials were likely to be donor species. They found n-type doping difficult in a mercury atmosphere, and proposed the absence of Hg_i for one of three reasons:

a) Hg_i is energetically unfavourable.
b) Hg_i is electrically inactive
c) Hg_i is extremely mobile and no non-equilibrium concentration may be maintained.

Vydyanath suggested that n-type doping in CMT was not due to Hg_i, but to the presence of an extrinsic impurity with a concentration below that detectable. For comparison, the conduction type of the II-VI compound ZnSe (Pautrat, 1982) has been found to be entirely due to small concentrations of impurities. Type conversion during an anneal in ZnSe is thought to be due to the diffusion of the impurities between a precipitate phase and the semiconductor matrix. Because precipitates of Te occur in CMT, this mechanism could occur here: the precipitates could contain a donor impurity, released upon their dissolution. For example: Yoshikawa et al. (1985) investigated oxygen contamination of CMT and concluded that oxygen was a donor impurity. By way of comparison, Nimtz et al. (1979) have observed n-p conversion in samples which had merely been stored for five years; Young and Giess (1991) found the effect after only a month.

2.2.2.2 By Extended Defects

It would seem that doping can also be caused by extended defects, including free surface. Surface n-type conduction in otherwise p-type samples of CMT was observed by Scott and Hager (1971). Raccah and Lee (1983) ascribed surface n-type conduction to defects caused by the stress of cleaving and polishing a surface. They claimed that n-type surfaces were deficient in mercury and contained few extended defects. Amirtharaj et al. (1985) commented that surfaces prepared by a bromine-in-methanol etch were of poor quality. Bromine-in-methanol is a very common planar etch for CMT. The basis of their work was a previous investigation of CdTe (Amirtharaj et al. (1984)); and there are other independent studies (Talasek et al. (1985), Lastras-Martinez et al. (1982)) which have reached the same conclusion by different means. Blomfield et al. (1994) have proposed alternative etches.

Gasan-zade et al. (1989) observed p-n conversion of CMT after plastic deformation, suggesting electrical activity of dislocations, but the work of Tregilgas (1988) would seem to disagree. Barbot et al. (1990) observed p-n conversion during deformation of material of high Cd content but not in pure CdTe.

Grain boundaries in CMT are known to be strongly n-type: Kraak et al. (1990) observed a 'two-dimensional electron gas' at the grain boundaries of p-type bicrystals. They suggested that the segregation of impurities might be the cause of this. Pogrebnyak et al. (1988) suggested the same for sub-grain boundaries. Klimakow and Schenk (1989) observed rapid grain-boundary diffusion of mercury in CMT, and suggested that enhanced mercury concentrations at grain boundaries might cause the observed p-n conversion.

2.2.2.3 Role of Tellurium Precipitates

Schaake & Tregilgas (1983) have studied tellurium precipitates in relation to type conversion during annealing. The precipitates would dissolve at 250-300^{o}C in an Hg atmosphere. During this dissolution, dislocations multiplied and climbed. Prismatic punching of dislocation loops occurred. A precipitate free n-type 'skin' with a sharp boundary between 'skin' and 'core' was observed. A p-n junction was observed at the boundary. If the dopant was a species diffusing between surface and boundary, the junction would instead be expected some way into the skin. (Schaake et al. (1985)).

Tregilgas et al. (1985) observed n-p re-conversion when the core region was completely dissolved in their samples, and so postulated an acceptor impurity which was expelled from the skin into the core, and which redistributed itself when the core was eliminated, instead of donor impurities released from the Te precipitates upon their dissolution.

Schaake et al. (1985) examined the rate of skin formation. Skin depth was proportional to $t^{\frac{1}{2}}/C^{\frac{1}{2}}$, where t was the diffusion time and C was the concentration of tellurium in the material above that required for stoichiometry. The results of Bogoboyashchii et al. (1985) agreed with these but the two groups did not acknowledge one another. Bogoboyashchii's work, moreover, concluded that:

> '... the rapidly diffusing defects are Hg_i ... in a medium with randomly distributed low-mobility 'traps' in the form of mercury vacancies ...'

whereas Schaake's concluded that the traps were tellurium precipitates.

The present author assumes the relation between skin depth and time may be derived as follows:

Let the initial concentration of sinks for the diffusing species be C.

Let the concentration of diffusing species at depth x and time t be $f(x,t)$.

Let the flux of diffusing species be $J(x,t)$.

Let the surface be at $x=0$.

Let no diffusing species pass a sink without reacting.

Let the depth of the skin-core boundary be at $x=d(t)$: so $f(d,t) = 0$.

Let $f(0,t) = C_0$, constant at the surface.

Let the diffusion coefficient be D, independent of f.

If dd/dt is small, the diffusion is approximately steady state. Then $df/dt_x = 0$. Fick's 2nd law gives:

$$df/dt_x = -dJ/dx_t. \quad ...(2.8)$$

So $dJ/dx_t = 0$, i.e. the diffusional flux is constant throughout the skin.

Fick's 1st law, $J = -D\, df/dx_t$, integrates easily:

$$Jx = -Df + A, \text{ where A is a constant.} \quad ...(2.9)$$

The boundary conditions are:

when $x = 0$: $0 = -DC_0 + A$ ...(2.10)
when $x = d$: $Jd = A$ ...(2.11)

so $J = DC_0 / d(t)$. ...(2.12)

The traps are filled at a rate dependent on the flux and their concentration:

$dd/dt = J / C$. ...(2.13)

Substituting:

$d\, dd/dt = DC_0 / C$ ...(2.14)

Integrating:

$d^2 = 2DC_0t / C + B$, where B is a constant. ...(2.15)

As $d = 0$ when $t = 0$, $B = 0$. ...(2.16)

By inspection, d is proportional to $t^{\frac{1}{2}} / C^{\frac{1}{2}}$. ...(2.17)

2.2.2.4 Interpretation by the Present Author

It occurs to the present author that the only possible surface mercury vapour reactions not including antisite defects are:

$Hg_{(g)} + V_M = Hg_M$ ...(2.18)
$Hg_{(g)} = Hg_M + V_{Te}$ (Lattice Building) ...(2.19)
$Hg_{(g)} = Hg_i$. ...(2.20)

Surface metal vacancy concentrations can in theory be made very high; the lowest possible concentration is zero. As diffusion rate is proportional to concentration gradient, this means that vacancy in-diffusion is bound to occur much faster than out-diffusion. This is analogous to the behaviour of carriers at a p-n junction in a semiconductor: flow is rectified.

It also occurs to the present author that the possible bulk vacancy - tellurium reactions may be summarised as follows:

(a) $Hg_i + Te_{(s)} = HgTe$ (as postulated by Schaake and Bogoboyashchii (1985)) ...(2.21)

(b) $Hg_i + V_M = Hg_M$ ...(2.22)

(c) $Te_{(s)} = Te_{Te} + V_M$. ...(2.23)

With the inclusion of (2.23) above, one can reconcile the models of Schaake (1985) and Bogoboyashchii (1985), that mercury in-diffusion occurs via Hg_i captured by Te precipitates and mercury vacancies respectively, because mercury vacancy concentration and Te precipitate concentration are related by:

$$[V_M] = k[Te_{(s)}]. \quad ...(2.24)$$

This relation then also offers an explanation for the identity of the junction with the skin-core boundary. Ironically, Schaake and Tregilgas (1983) discuss a form of this reaction briefly.

2.2.3 Impurity Segregation

Schaake et al. (1984) discussed four mechanisms of impurity redistribution in relation to type conversion:

a) Strain gradient redistribution (e.g. to dislocation cores).

b) Segregation between phases

c) Impurity distributions must be affected by defect distributions where impurities and defects form complexes.

d) Interaction with conduction type in semiconductors; e.g.: Cu will diffuse to p^+ regions of Si.

This last is similar to the phenomenon of 'self-compensation', where dopant impurities affect the distribution of native defects.

The authors claimed that none of the above could explain silver diffusion in CMT. When Hg diffused in, Ag diffused away from the source of Hg. They instead considered 'kick-out' diffusion:

$Hg_i + Ag_M = Hg_M + Ag_i$, ...(2.25)

i.e., $[Ag_i] = [Hg_i][Ag_M]$ in equilibrium. ...(2.26)

If $[Hg_i]$ is a fixed function of position and $[Ag_M]$ is initially constant, $[Ag_i]$ becomes proportional to $[Hg_i]$. These Ag_i will diffuse until $[Ag_i]$ is constant. $[Ag_M]$ will then be inversely proportional to $[Hg_i]$. That is, the Ag will segregate away from the source of Hg_i. Schaake et al. (1985) showed that the same equilibrium and consequent segregation could occur when Frank-Turnbull diffusion was active.

Goesele et al. (1980) suggested that one could distinguish between Frank-Turnbull and kick-out diffusion. Brown and Willoughby (1983) claimed that Frank-Turnbull diffusion was dominant in CMT. Support for this conclusion may be found in Jones et al. (1983), but these authors derived no theoretical conclusion from their work. Pain (1992) proposed $Hg_i^{\cdot\cdot} + Hg_M = (Hg_2)_M^{\cdot\cdot}$, where $(Hg_2)_M^{\cdot\cdot}$ is a particular form of metastable interstital.

2.2.4 Effect of Dislocations on Diffusion

Archer et al. (1985-1993) observed enhanced diffusion rates, or 'pipe-diffusion' along dislocations. Pipe-diffusion can lead to diffusion profiles which do not fit a standard 'error' function curve. As follows, many

Soviet researchers have worked on diffusion and have observed many diffusion profiles which did not fit a standard error-function curve, but in the most part they have been unable to observe 'short-circuit' diffusion in the same way as Archer et al. (1985-1993).

Zaitov et al. (1973-1974) found that iridium but not silver or cadmium diffused inhomogeneously in CMT under an applied electrical field.

Gorshkov et al. (1984) examined ^{203}Hg, ^{64}Cu, ^{110}Ag, ^{198}Au, ^{113}Sn, ^{32}P and ^{125}Sb, and observed error-function diffusion profiles for the p-block elements but not for the d-block elements; however, the authors could detect no inhomogeneity of diffusion. This group also found that diffusion coefficients could be reduced by indium doping.

2.2.5 Dislocation Charge

Experiments to determine the set of the mobile dislocations have often involved the measurement of dislocation charge, the existence of which is inferred when either a potential difference or a current is produced during plastic deformation.

If the polarity of the charge carried by a dislocation is a function of its type (i.e., the species of atom in excess at its core), then the direction of charge flow during slip should be a function of the mobile dislocation set. So Speake et al. (1978), by assuming that Zn and S dislocations in ZnS carried positive and negative charges respectively (inferred from the ionicity exhibited by isolated Zn^{2+} and Te^{2-} species), could say that the mobile dislocations were glide-set, as they expected. If one knew independently (by the observation of partials in TEM, for example) that the glide-set dislocations were dominant, one would be able to deduce the associated charges of the two types.

2.2.5.1 Time Dependence of Dislocation Charge

Dislocation charge has been found to increase with strain rate. Kirichenko and Petrenko (1980) found that the current responded slowly to transient changes in strain rate, and found no Hall voltage across their sample. Osip'yan et al. (1986) wrote:

> 'The abrupt fall in the apparent dislocation charge at the lowest strain rates has been attributed to the screening of the dislocation charge by a cloud of point defects which at low velocities can move with the dislocation...'

but they were more interested in the 'photoplastic effect' where stress is dependent on both strain rate and illumination.

Pellegrino and Galligan (1988) supported the view that Peierls stress was dependent on dislocation charge, and that the carriers produced by irradiation caused the increase in flow stress. They injected carriers at sample surface, whence they had to diffuse to influence dislocation motion: thus they explained a delay between illumination and any change in stress proportional to $e^{-1/T}$, where T is absolute temperature. But they also observed a polymodal distribution of delay times, which they could not explain.

Garosshen et al. (1990) observed an increase in current with illumination, and an increase in the photoplastic effect with strain rate, thereby supporting the model of Osip'yan (1986) that dislocations 'sweep up' carriers.

Kung et al. (1992) found an increase in current with specimen resistivity; Carlsson and Ahlquist (1972) found a decrease in yield stress and photoplastic effect. These last controlled resisitvity by varying stoichiometry by reaction with the gas phase.

Marschall & Milstein (1993) and Garosshen et al. (1990) observed the photoplastic effect in slip systems where, because of symmetry, the dislocations had no type.

2.2.5.2 Interpretation by the Present Author

Osip'yan et al. (1986) drew a schematic diagram of the structure of CMT in (110) projection, to illustrate glide on a shuffle plane:

```
@@@@@@@@@@@@@@@@@   -¼s         @@@@@@@@@@@@@@@@@@   -¼s
+   +   +   +   +               +   +   +   +   +
 -   -   -   -   -               -   -   -   -   -

 +   +   +   +   +               +   +   +   +   +
  -   -   -   -   -               -   -   -   -   -
....................      =    ........................
  +   +   +   +   +           +   +   +   +   +
   -   -   -   -   -           -   -   -   -   -

   +   +   +   +   +           +   +   +   +   +
    -   -   -   -   -           -   -   -   -   -
    *****************   +¼s    *****************   +¼s
```

where '+' is a metal ion, '-' is a tellurium ion, and '@' and '*' represent the surface charges which exist to balance the overall dipole moment of the ions, which may be calculated as follows:

Let 's' be the magnitude of the charge density per unit area of a plane of ions parallel to the slip plane.

Let 'a' be the repeat distance normal to the slip plane.

The structure is a series of plane-pairs, the separation between halves of a pair being $\frac{1}{4}a$.

Therefore the dipole moment of each pair per unit area is $\frac{1}{4}as$.

For a series of n pairs, the dipole moment is $\frac{1}{4}asn$.

The height of such a series is an.

Thus compensating charges of magnitude $\frac{1}{4}s$ separated by na can reduce the external dipole moment of the structure to zero. This is what is illustrated above.

However, by this argument the following sketch of the structure is valid:

```
*****************   +¾s
-   -   -   -   -


+   +   +   +   +
 -   -   -   -   -
.....................
 +   +   +   +   +
  -   -   -   -   -


  +   +   +   +   +
  @@@@@@@@@@@@@@@@@   -¾s
```

The surface charges will balance the dipole moment of the ions in a crystal of any shape if each element of surface has an associated surface charge dependent on its structure: from the above examples, unicoordinate surfaces and tricoordinate (111) surfaces have charge densities of magnitude $\frac{3}{4}s$ and $\frac{1}{4}s$ respectively.

It occurs to the present author that in this localised charge model, the following sketch is valid:

```
@@@@@@@@@@@@@@@@@@  -¼s      @@@@@@@@@@@@@@@@@@  -¼s
+   +   +   +   +            +   +   +   +   +
 -   -   -   -   -            -   -   -   -   -

 +   +   +   +   +            +   +   +   +   +
  -   -   -   -   -   -¼s  @@@@-   -   -   -   -
.....................   =  .........................
  +   +   +   +   +        +   +   +   +   +****  +¼s
   -   -   -   -   -        -   -   -   -   -

   +   +   +   +   +        +   +   +   +   +
    -   -   -   -   -        -   -   -   -   -
   ******************  +¼s  ******************  +¼s
```

This modification to Osip'yan's illustration now indicates electronic flow between opposite faces of a deforming crystal.

If this charge flow is conducted through an external circuit, no Hall voltage is expected within the sample, as observed by Kirichenko and Petrenko (1980).

The voltage across an open-circuited sample can be calculated as follows.

Let E be the shear strain of the crystal

Let t be time

Let R be the resistance, V the potential difference and C the capacitance of the crystal between the two faces between which the charge is to flow.

Let Q be the magnitude of the unbalanced charge per unit area on the faces between which charge is to flow.

Let a be a measure of the surface charge of a surface revealed by slip

Unbalanced charge is increased by a change in shear strain, and decreases by flow through the resistance of the crystal under the potential difference caused by its separation across the capacitance. By inspection:

$$dQ/dt = a(dE/dt) - Q/RC \quad ...(2.27)$$

For constant dE/dt,

$$-RC \ln (a(dE/dt)RC - Q) = t + k \quad ...(2.28)$$

where k is a constant. If $Q = 0$ when $t = 0$,

$$Q = a(dE/dt)\ RC\ (1 - e^{-t/RC}) \quad ...(2.29)$$

or $$V = a(dE/dt)\ R\ (1 - e^{-t/RC}) \quad ...(2.30)$$

For large t,

$$V = a(dE/dt)\ R. \quad ...(2.31)$$

V is increased by an increase in crystal resistance or strain rate, as observed by Kirichenko and Petrenko (1980) and Kung et al. (1992) respectively.

Thus a model which includes localised surface charge is compatible with the experimentally observed results.

A model for the localisation of charge on dislocations then becomes obvious:

```
  -¼s @@@@@@@@@@@@@@@@@   -¼s @@@@@@@@@@@@@@@@@
      +   +   +   +   +       +   +   +   +   +
       -   -   -   -   -       -   -   -   -   -

       +   +   +   +   +       +   +   +   +   +
        -   -   -   -   -       -   -   -   -   -
-¼s @@@@................... = .....................
    +   +   +   +   +**** +¼s   +   +  + +  +**** +¼s
     -   -   -   -   -           -   -  - -  -

     +   +   +   +   +           +   +  + +  +
      -   -   -   -   -           -   -  - -  -
      ***************** +¼s       ************* +¼s
```

In this model, dislocation charge is associated with the destruction or creation of surface steps, which in turn is associated with only the edge components of dislocations. This is in agreement with the observation of Osip'yan et al. (1986) that only edge dislocations carry charge.

Dislocations act as recombination centres by introducing localised deep levels into a material (Tregilgas (1982), Moore and Schaake (1983), Nakagawa et al. (1979) and Titchmarsh et al. (1977)). The localised charge model above would require these levels to be occupied by charge carriers. Illumination can obviously change the occupancy of such levels and redistribute charge carriers between these localised levels and the conduction and valence bands of the parent material. This may contribute to the photoplastic effect in this material.

2.3 Mechanisms of Growth

2.3.1 Three Growth Models

In a particle of a solid phase bounded by other phases (other solids, liquids, gases etc.), the energies of atoms at the surface can be different to those of atoms at the centre, because the atoms at the surafce interact with atoms different to those at the centre.

For a spherical particle, the surface area is proportional to the square of the radius. The volume is proportional to the cube of the radius. In a very small particle, therefore, the mean energy per atom tends towards that of a surface atom. In a larger particle, the mean energy per atom tends towards the energy of an atom at the centre.

If the energy of an atom at the surface is higher than that of an atom in the centre, a particle has minimum energy if it is spherical, assuming that surface energy is isotropic. Therefore, if the energy of a surface atom is higher than that of an atom in the centre, a particle will have a higher mean energy per atom when it is smaller.

When a compound solidifies, small particles must be formed first. These particles will enlarge with time. In a compound where surface energy is higher than bulk energy, as described above, the particles will be spherical and the mean energy per atom of each particle will reduce with time. Thus it is in general more energetically favourable to enlarge an existing particle than to form a new one.

The solidification of such a compound may therefore be divided into two phases:

a) 'Nucleation', when the distribution of particles is decided.

b) 'Growth', when they enlarge with time.

If a compound nucleates and the phase it is in contact with causes it to have lower surface energy per atom than bulk energy, the compound will be lamellar to maximise its surface area and thus minimise its mean energy per atom.

When a compound nucleates on a solid surface 'substrate' (in general, the interface of two phases), the shape of the nuclei is a function of three energies:

a) The surface energy of the new phase
b) The surface energy of the substrate
c) The energy of the 'heterointerface' between the nucleus and the substrate.

Because energy is transferred when a surface changes area, surface energy can be represented as a surface tension.

In a physical system, three surfaces can meet only at a line. This is illustrated in Figure 2.2. The angles at which the surfaces meet in equilibrium are determined only by the shape of the substrate and their relative surface energies. It can be seen that:

1. If the surface energy of the uncovered substrate is higher than the sum of the other two energies, the phase will nucleate as a single atomic layer covering the substrate.

2. Otherwise, nuclei will have one planar surface (substrate side) and one curved surface (gas/liquid side), which meets the substrate at the required angle for a balance in surface energies.

3. After the substrate has been completely covered in (1), the influence of its surface energy is removed and growth may proceed as in (2).

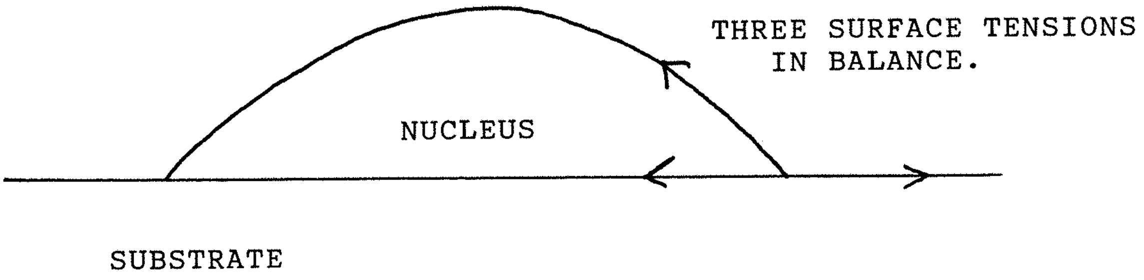

Figure 2.2: General form of a nucleus of a phase being deposited on a planar substrate.

These three possibilities have been considered by Frank and van der Merwe, Stranski and Krastanov, and Volmer and Weber respectively, and are called the 'F-vdM', 'S-K' and 'V-W' models. The last two are commonly classified together as 'island' or '3-D' growth.

A substrate which is not uniform may have areas which promote the formation of nuclei.

2.3.2 Kinetics of Growth

These models assume that growth species are easily availble. It is commonly assumed instead that growth species arrive at the surface and diffuse for a time while 'adsorbed' until they either reach a site at which their energy is reduced, or they are 'desorbed'. One type of site which causes energy reduction is the edge of a growing nucleus. An adsorbed species therefore has three options:

1. Desorb
2. Add to a growing nucleus
3. Stop somewhere else and become a new nucleus.

The mobility and incident flux of the adsorbed species can alter the balance between (2) and (3) in this list. Mobile surface species encourage F-vdM growth, while poorly mobile species encourage 'island', or 'three-dimensional' growth in either the S-K or V-W mode.

2.4 Relaxation

Relaxation is an interaction of defects with strain. Specifically, it is the process whereby a strained coherent epitaxial layer (section 2.1.7) can become a semicoherent layer with less strain.

The dislocation structure of an epitaxial layer can be produced by relaxation. Two well-known examinations of this have been published by van der Merwe (1949, 1991) and Matthews and Blakeslee (1970, 1974). It is the belief of the present author that their work may best be illustrated for the purposes of this thesis by following similar, but simplified reasoning through to its logical conclusion, as follows. This work illustrates that their arguments need not be presented in an overtly mathematical manner to achieve valid and consistent results.

The interface between two solid phases can be roughly classified into one of three types:

a) Coherent: the lattice parameters of the two phases in the plane of the interface are equal, or in the ratio of small integers, so that the interface structure repeats over a distance comparable to the lattice parameters of the phases. In general, for phases whose lattice parameters do not satisfy the above condition, both will be elastically strained. The division of the strain between the two phases depends on their relative thicknesses.

b) Semi-coherent: the lattice parameters of the two phases in the plane of the interface differ from that required for coherency. The interface contains an approximately uniform network of dislocations to accomodate extra half-planes in one of the phases.

c) Incoherent: as (b), but the structure of the interface cannot be described in terms of a network of dislocations.

If one phase is thicker than the other to a sufficient extent, when both layers are strained the strain in the thicker layer will be negligible. This is the case in the layers examined in the present work: the strain in the substrate is negligible.

The network of dislocations in a semi-coherent interface has an energy which increases with its dislocation density, which by inspection is proportional to the amount of strain which it accommodates. A uniformly strained layer has a strain energy which is proportional to its thickness and the square of its strain. To minimise energy the dislocation density of the interface between a thin layer and its substrate is expected to be lower than that of a thicker layer. As a layer is deposited, then, dislocations are introduced at the interface. There are three possibilities:

a) Dislocations move in from the surface
b) A dislocation loop is created at the interface, which expands until half of it is expelled from the surface.
c) A dislocation loop in the bulk of the layer expands towards the surface and the interface.

When an edge dislocation of a sign which allows strain accommodation reaches the heterointerface, most of the strain associated with the dislocation relaxes. When any dislocation reaches the surface of a sample, all the lattice strain associated with it relaxes. Conversely, energy must be supplied to expel a dislocation from these regions. Thus dislocations are attracted to free surface and, by inference, to the heterointerface if they are of the appropriate sign.

There is, therefore, an activation energy for the introduction of a dislocation at the heterointerface, roughly equal to the energy of a dislocation in the bulk. This must be supplied by the strain in the layer. Therefore the following can be seen to apply at equilibrium:

$$\text{Energy of a bulk dislocation} - \text{Reduction in strain energy caused by the creation of one interface dislocation} = \text{zero} \qquad \ldots(2.32)$$

The energy of a bulk dislocation is a constant, k_d.

By definition, the change in strain energy with strain is equal to the stress i.e. strain x elastic constant.

The reduction in strain caused by the introduction of one dislocation per unit length is equal to b, the magnitude of the Burgers' vector of the dislocation. This is a small quantity and therefore it can be assumed that the strain energy varies linearly over this change.

So, the reduction in strain energy caused by the introduction of one dislocation per unit length at the heterointerface of a strained layer is:

$$bk_st(a_1 - a_0) / a_0 \qquad \ldots(2.33)$$

where k_s is the elastic constant of the layer, t is its thickness, a_0 is its lattice parameter when unstrained, and a_1 is its lattice parameter when strained. As b is approximately equal to a_0 this simplifies to:

$$k_st(a_1 - a_0). \qquad \ldots(2.34)$$

Thus at equilibrium,

$$k_d = k_st(a_1 - a_0). \qquad \ldots(2.35)$$

Let a_2 be the lattice parameter of the substrate. When the layer is fully relaxed, $a_1 = a_0$. But as a_1 approaches a_0, t approaches infinity. This implies that no layer is ever fully relaxed. When the layer is fully coherent, $a_1 = a_2$ and the equation becomes:

$k_d = k_s t(a_2 - a_0)$.   ...(2.36)

Now $(a_2 - a_0)/a_0$ is a measure of the 'misfit' between a layer and its substrate, m. Substituting and rearranging:

$t = k_d / k_s a_0 m$ ...(2.37)

This shows that a layer can be fully coherent below a certain thickness.

In summary,

1. No strained epitaxial layer ever becomes fully relaxed.

2. Epitaxial layers will have coherent interfaces with their substrates below a thickness $t = k_D/k_S a_0 m$, where k_D is the energy of a dislocation per unit length, k_S is of the order of the Young's modulus of the layer, a_0 is the lattice parameter of the layer and m is a measure of the misfit between the layer and the substrate.

2.4.1 Energy Required to Introduce a Dislocation

It is obvious from the literature and this discussion that the energy of dislocations in a layer has an effect on the relaxation of that layer.

The strain energy per unit length of a screw dislocation is calculated in many undergraduate texts, by assuming that the problem has radial symmetry. The result is that:

$k_d = (Gb^2/6.28) \ln(r_1/r_0)$ ...(2.38) where r_1 is an arbitrary radius at which the influence of the dislocation is negligible (i.e., the distance to an interface or another dislocation) and r_0 is an arbitrary radius, called the 'core radius', below which the relation between stress and strain becomes non-linear due to the magnitude of the strain and the atomic nature of the material. G is the elastic shear modulus of the material.

At first sight, no symmetric solution exists for an edge dislocation. However, a solution may be derived by inspection as follows:

Consider a screw dislocation along the z-axis of a cartesian coordinate system. Only two strains need exist: shear on the x-plane in the z-direction and on the y-plane in the z-direction: s_{xz} and s_{yz} respectively.

Lines of atoms in the x- and y-directions are bent by these strains along the z-axis. The displacement between opposite ends (at infinity) of a line of atoms is by inspection equal to half the Burgers vector b. This may be represented by integrals:

The integral over all x of s_{xz} dx = ± b/2 (2.39)
" " " " y of s_{yz} dy " " " (2.40)

In an edge dislocation also, only two strains are necessary. Using the notation above,

The integral over all x of s_{xx} = ± b/2 ...(2.41)
" " " " y of s_{xy} " " " ...(2.42)

So a valid strain field for an edge dislocation may be produced from that for a screw dislocation by replacing s_{xz} by s_{xx} and s_{yz} by s_{xy}.

By symmetry, the contributions to the energy of a screw dislocation from s_{xz} and s_{yz} must be equal to each other and to $(Gb^2/12.6) \ln (r_1/r_0)$ ...(2.43)

By inspection, the energy of an edge dislocation is then:

$$k_d = ((E + G)b^2/12.6)\ \ln(r_1/r_0). \quad ...(2.44)$$

where E is the Young's modulus of the material

The elastic moduli of a material are constant, as is the core radius r_0. The value of r_1 is the distance from the dislocation at which the strain becomes negligible: at an interface or another dislocation perhaps.

Thus as a layer gets thicker, the energy of a dislocation in it will increase (and thus dislocations are attracted to free surface). If the dependence is approximately logarithmic, the dependence will be weak in thick layers. However, there are other obvious factors which influence the energy required to introduce a dislocation at the interface between a layer and its substrate, as follows:

2.4.2 Work Done Against Peierls Stress

The work done against Peierls stress must increase linearly with thickness. Assuming that dislocations can move normal to a layer, the work U_p done against a Peierls stress P when one dislocation with Burgers vector of magnitude b is moved through a layer of thickness t is:

$$U_p = Pbt \quad ...(2.45)$$

A constant would be introduced if glide were on planes which were not normal to the layer surface.

With this correction, the energy k_d required to introduce a dislocation at the heterointerface is:

$$k_d = k_1 a_1{}^2 + Pbt \quad ...(2.46)$$

where $k_1 = f(G, E, r_1, r_0)$ ...(2.47)

From above, for an unrelaxed layer,

$$t = k_d / k_s a_0 m. \quad ...(2.48)$$

By substitution,

$$t\ (k_s m - Pb) = k_1 a_1{}^2. \quad ...(2.49)$$

This suggests that a layer will never relax if $k_s m$ is less than P. Interestingly, the constant k_1 does not appear in this equation. Even if, as implied above, dislocation energy becomes very small in a thin layer (a logarithmic increase with thickness) this prediction would seem to be valid.

The above result may be confirmed by inspection as follows. The change in strain energy with dislocation density is proportional to both strain and layer thickness. The work done against Peierls stress per dislocation is proportional to layer thickness. Thus the work done against Peierls stress per dislocation can be greater than the reduction in strain energy if the strain in the layer is sufficiently small, for a layer of any thickness.

In CMT, the yield stress is about 5MPa; the Young's modulus is about 50GPa. Assuming that Peierls stress is of the order of yield stress, and that the required elastic constant k_s is of the order of the Young's modulus, it may be calculated that a layer of CMT will not relax if its strain when coherent with its substrate is less than 0.01%.

Tobin et al. (1995) observed that a layer of CMT on cadmium zinc telluride did not relax when the strain in the layer was less than 0.003%. This value is within an order of magnitude of that predicted by the above simplistic analysis, supporting the route taken and the physical assumptions used.

2.4.3 Relaxation of 14% Misfit

CdTe has 14% misfit with a GaAs substrate. The critical thickness t was estimated above as:

$$t = k_d / k_s a_0 m. \qquad \ldots(2.50)$$

This formula neglects any effect of Peierls stress. Peierls stress is unimportant here because it can be assumed that the layer will relax when it is very thin.

From above, the energy of a bulk dislocation, k_d, is given by:

$$k_d = (Gb^2 / 6.28) \ln(r_1 / r_0). \qquad \ldots(2.51)$$

It is obvious that this equation is inapplicable to dislocations in very thin layers. If one assumes the logarithmic term is unity,

$$t = Gb^2 / 6.28 k_s a_0 m \qquad \ldots(2.52)$$

If we approximate $G = k_s$ and $b = a_0$,

$$t = b / 6.28m \qquad \ldots(2.53)$$

so t is approximately equal to b. That is, the layer will relax when it is a single atomic layer thick. This implies that the logarithmic term should have been taken as zero: or, rather, that this formula for the energy of a dislocation is inapplicable to the relaxation of 14% strain.

3. EXPERIMENTAL

The results to these experiments are collected together in Chapter 4.

3.1 Materials for Study

Five material systems were examined. Each was prepared by one or the other of the following methods:

1. Liquid-phase epitaxy, 'LPE'. This is in general where a layer is formed by the solidification of a melt on a suitable substrate. Here the substrate was cadmium zinc telluride and the melt was rich in tellurium.

2. Metal-Organic Vapour-Phase Epitaxy, 'MOVPE'. This is where a suitable substrate is exposed to vapourised organic compounds of the constituent elements of the layer to be deposited. The layer is formed when the vapours decompose. Here, the mercury source was elemental mercury and the cadmium source was dimethyl cadmium, $(CH_3)_2Cd$. Two tellurium compounds were used: di-isopropyl tellurium ('DIPT', pronounced 'dipped'), $((CH_3)_2CH)_2Te$ and methyl allyl tellurium ('MATe', pronounced 'matey'), $CH_3TeCHCH_2$.

The five materials were as follows:

Material 'A'

This was MOVPE CMT (x about 0.2) deposited on a CdTe 'buffer layer'. MATe was used to deposit the CdTe and DIPT was used to deposit the CMT. The substrate was GaAs, cut 2° off (001) towards (110).

Material 'B'

Material 'B' was a 'buffer layer' of CdTe, deposited using DIPT on the same substrate as material 'A'.

Material 'C'

Material 'C' was identical to material 'B' in all respects except that MATe was used in the deposition. Material 'C' is an intermediate stage in the production of material 'A'.

Material 'D'

Material was LPE CMT on (111) (Cd,Zn)Te

Material 'E'

Material 'E' was MOVPE $Cd_xHg_{1-x}Te$ deposited on CdTe prepared as in material 'C'. As the CMT was deposited, the doping level and the value of 'x' in the formula were varied. First, the material was p-type and high 'x' (0.34); then, low n-type low-x (0.17) material was deposited; finally, strongly n-type high-x (0.225) material was deposited.

All deposition was performed using proprietary techniques by GEC-Marconi Infra-Red Ltd. of Millbrook, Southampton. The manufacturers were not forthcoming with detailed information about their preparation routes, and so the above cursory description of the samples can serve only as an index. However, detailed knowledge of manufacturing routes is irrelevant to the following phenomenological study, which, it will be seen, seeks to define samples in terms of their microstructures.

3.2 Optical Microscopy

In MOVPE, a gallium arsenide substrate can be used. Before any CMT is deposited on this, a 'buffer layer' of CdTe is deposited. The quality of the CMT depends on whether DIPT or MATe is used in the deposition stage. (Capper, P., private communication) CMT on DIPT CdTe (Material 'A') is known to possess 'hillocks'. Observation of these was thought to be an easy initial challenge.

Material 'A' was examined with an optical microscope (Figure 4.1). The same area was then examined with Nomarski Differential Interference Contrast ('DIC'), Figure 4.2.

To obtain cross-sectional information, a piece of material 'A' was then cleaved along a natural cleavage plane by the application of gentle pressure across the edge of a microscope slide, and the freshly cleaved surface was observed with Nomarski DIC (Figure 4.3), to see if the hillock had caused deviation of the fracture plane.

3.3 Etching

3.3.1 Experiments to Selectively Etch CMT with Hillocks

Chemical etches can be sensitive to microstructure. A solution of elemental bromime in methanol is a well known (Chapter 2) planar etch in CMT. An etch which is known to be selective is after Polisar. This 'recipe' for 'Polisar 2' is copied verbatim from Brown and Willoughby (1979):

Component	Quantity
'Conc. HNO_3'	60 cc
'Conc. HCl'	25 cc
H_2O	60 cc
'Acetic acid'	5 cc
Br_2	0.1 cc

Many references are ambiguous in a similar manner. For our work, the components were chosen from easily available standards as follows:

Component	Density / kgl^{-1}	Molarity / $moll^{-1}$
'Conc. HNO_3'	1.42	15.5
'Conc. HCl'	1.18	11.5
'Acetic Acid'	1.05	17.4

Figure 4.4 shows a typical result of an etch in Polisar 2 prepared as described above. Etching occured predominantly at the top edge of each hillock.

To test for the presence of topological effects, a fresh sample of this material was etched in a solution of Br_2 in methanol (1% by volume) until no sharp edges were visible on the hillocks. Then the samples were etched in Polisar 2. Figure 4.5 shows that the same defects were revealed.

3.3.2 A new etch.

The potential of the Polisar etch for revealing defects associated with hillocks was explored further. First, the mixture was simplified to one of equal parts HNO_3 and H_2O by volume. This concentrated acid attacked the CMT but left a brown stain.

Brown and Willoughby (1979) suggested that staining etches should be followed by an etch in Bromine/Methanol solution. Here, it was found that the staining did not occur if a thousandth part by volume of Br_2 (elemental liquid) was added to the acid. This etch did not however reveal any defects.

All the preferential etches reviewed by Brown and Willoughby (1979) contained chloride, added in the form of hydrochloric acid. Chloride in a similar proportion to that in these etches was added to the mix. The mixture can be summarised as follows:

Component	Density gcm^{-3}	Molarity moll^{-1}	Proportion	Molarity moll^{-1}
HNO_3	1.42	15.5	60	7.25
HCl	1.18	11.5	8	0.72
Br_2	3.14	19.6	0.12	0.02
H_2O	1.00		60	

Figure 4.6 shows the results of an etch of Material A in this mixture. More linear features may be seen in this micrograph than in Figures 4.4 or 4.5. Some of these are associated with very faint features of the same shape as the hillocks but with reversed contrast - i.e., they are shallow, hillock-shaped depressions in the surface.

3.3.3 Experiments to Etch a Bevel to Reveal Material at All Depths in a Sample of CMT

Bevel etching is the etching of a sample for a time which is a function of position. In a planar etchant, for example bromine/methanol in this system, this produces a sample which is etched to a depth which is a function of position - i.e., a bevel. The technique can also be used to find the ideal etch time for a defect etch such as the modified Polisar etch described here.

Bevel etching is achieved by either the steady motion of a sample into a bath of etchant, or by the suspension of the sample over a bath of etchant the level of which is steadily rising. GEC-Marconi have used the latter technique with success. In their equipment there were no moving parts, flow rate being controlled with a PTFE needle valve. This equipment was further simplified for the present work. The apparatus is shown schematically in Figure 3.1. Flow was measured by measuring the frequency of drips from a spherical dropping funnel, whose large cross-section relative to that of the reaction vessel, a cylindrical funnel very slightly wider than a microscope

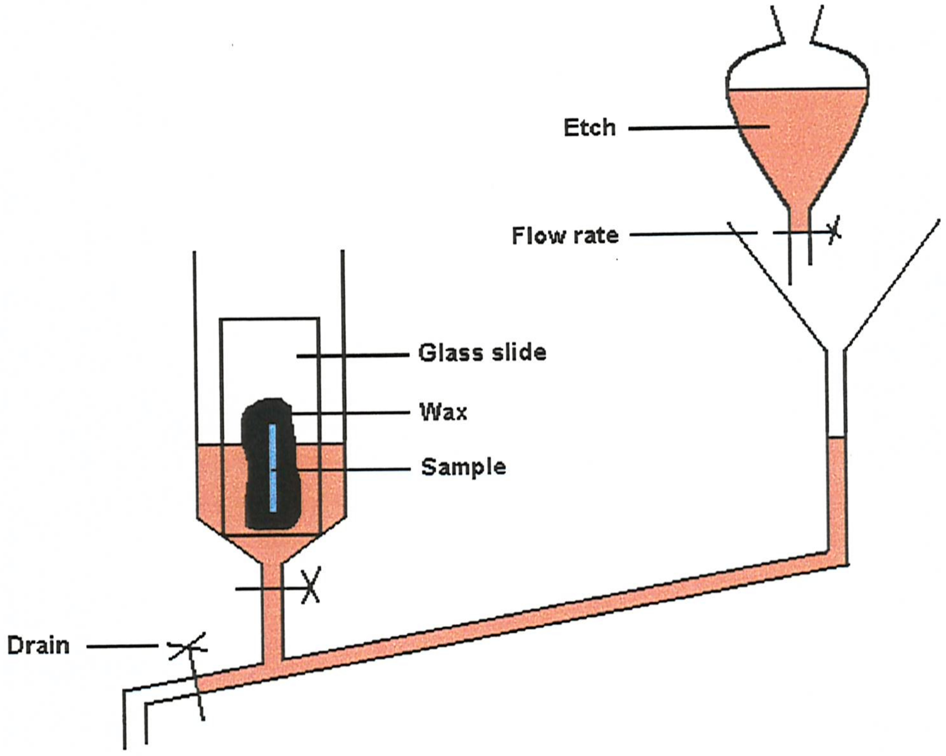

Figure 3.1: Apparatus developed by the present author for bevel-etching

slide so as to support such a slide nearly vertically, ensured a slow change in head, and therefore flow rate, with time. The drips were collected by a conical funnel where they passed through a U-bend of narrow pipe to the reaction vessel. The sample was supported on a microscope slide with a black wax which was not attacked by the etch.

A sample of material 'A' was cleaved by the application of light pressure across the edge of a microscope slide into a long strip about 2mm in width. This was bonded to a microscope slide with a chemically unreactive black wax, as above, by heating the slide to melt the wax.

The apparatus discussed above (Figure 3.1) was constructed, and the spherical dropping funnel was filled with a 1% by volume solution of bromine in methanol. The solution was allowed to drip from the dropping funnel into the apparatus, so that the sample became immersed in the solution over a period of about 10 minutes.

After being almost fully immersed, the sample was rinsed in excess water and allowed to dry. Then it was etched in the 'new etch' described above. The result was photographed and is shown in Figure 4.7.

3.4 White-Beam Synchrotron X-Ray Topography

Lamellar crystalline defects large enough to be revealed in the optical microscope by etching should be detectable by X-ray topography.

X-ray topography reveals defect distributions in a crystal by mapping the intensity of an X-ray reflection as a function of position. With synchrotron radiation, the entire crystal can be illuminated at once; otherwise, a scanning arrangement is used. In a perfect crystal, the diffracted radiation will be collimated. Photographic emulsion can then be used to record an image of the crystal. Because no lenses exist for X-rays, the resolution of the image is then limited to the resolution of the photographic emulsion, which is comparable to the wavelength of light. With a broad spectrum source of X-rays (a 'white beam'), reflection can occur in many directions from the crystal and therfore many images can be collected simultaneously with a sufficiently large photographic plate.

The images reveal defects as follows. Where a reflection from the matrix is reduced in intensity, there is a defect. When an image is distorted, the crystal is distorted. Where there is a break in an image, there is a slight, abrupt change in the orientation of the crystal, i.e. a sub-grain boundary.

Some defects (e.g. twins) give rise to reflections where there are none from the matrix, but at known positions relative to reflections from the matrix. These reflections show an increase in intensity where the crystal contains the defect to which they correspond.

Images can be collected using either 'reflected' or 'transmitted' X-ray reflections: those that leave the sample from the same face as the incident radiation, and those which pass through the sample respectively. In CMT, X-rays of certain wavelengths are absorbed within a few microns, and so a reflection topograph can be used to isolate the surface and bring no information from any dislocations at heterointerfaces. This technique was therefore chosen, with the emulsion plate centred on a matrix reflection as the nature of the defects it might contain were not known.

On the suspicion that the lamellar defects were twins (section 2.3.3), a reflection which was <u>not</u> present in a twin had to be chosen for maximum contrast. The other experimental constraints were as follows:

1.) MOVPE CMT has (001) surface, tilted 2^o towards (110).

2.) The lattice parameter of x=0.2 CMT, a = 6.465 Angstroms.

3.) The maximum wavelength of x-rays available from the synchrotron source (Daresbury) was 1.76 Angstroms.

4.) The incident angle should be as large as possible so that beam intensity is high, the illuminated area is easy to position, and there can be no topographical shadowing.

5.) The 'take-off' angle should ideally be 90^o, to avoid foreshortening of the image.

6.) The illuminated area should be small to reduce background scatter and prevent the overlap of images from adjacent reflections.

7.) The diffracting planes should ideally not be parallel to the surface so that the take-off angle can be close to 90^o. If the angle is greater than 45^o the reflection comes back towards the source.

Five low-order reflections were considered initially, to allow a 90^o take-off angle. For a 90^o take-off angle the conditions are as follows.

For planes with Miller indices (hkl), the plane spacing is $d = a / (h^2+k^2+l^2)^{\frac{1}{2}}$.

The angle between the plane normal and the surface normal, assuming the surface normal is (001), is $\cos^{-1}(l/d)$.

The diffraction angle theta and the incident angle are derived geometrically; the wavelength for the satisfaction of the Bragg condition may then be easily calculated.

Indices (hkl)	Spacing (Angstroms)	Angle to surface	Theta	Incident angle	Wavelength (Angstroms)
113	1.949	25.24°	64.76°	39.5°	3.53
226	0.975	25.24°	64.76°	33.7°	1.76
224	1.320	35.26°	54.74°	19.5°	2.16
335	0.986	40.32°	49.68°	9.4°	1.50
115	1.244	15.79°	74.21°	58.4°	2.39

Most of these reflections require long-wavelength radiation which the instrument is not suited to supply. For 1.76 Angstrom radiation,

Planes (hkl)	d (Angstroms)	Angle to surface	Theta	Take-off angle	Incident angle
113	1.949	25.24°	26.84°	52.1°	1.6°
224	1.320	35.26°	41.81°	77.1°	6.6°
335	0.986	40.32°	40.32°	103.5°	22.9°
115	1.244	15.79°	45.02°	60.8°	29.2°

(113) is clearly a borderline case, particularly when the +/- 2° misorientation of the (001) layer normal is included. But this was chosen as the first diffraction condition. A sample of material 'A' was sent to the National Synchrotron Radiation Source at Daresbury, and a reflection topograph was taken with the following conditions:

Miller indices of reflecting planes: (113)
Incident angle: 1.6°
Take-off angle: 52.1°
Radiation wavelength: 1.76 Angstroms

The resulting image was printed onto photographic paper and is shown in Figure 4.8.

3.5 Atomic Force Microscopy (AFM)

Materials 'B' and 'C' were buffer layers of MOVPE CdTe, a couple of microns thick on GaAs 2^{o} off (001) towards (011). These were studied to explore the differences between MATe and DIPT in the growth of buffer layers, and their effects on the hillock population of the final CMT layer. The CdTe of material 'B' was deposited using DIPT, and that of material 'C' was deposited using MATe. Material 'B' is, therefore, an intermediate stage in the production of material 'A'.

In the optical microscope, both layers appeared featureless. In the scanning electron microscope, faint structure was suggested but could not be resolved due to lack of signal, indicating extremely shallow surface features (Figures 4.9-4.10). It was thought that an atomic force microscope would be ideal for the examination of these.

Material 'D' was LPE material on (111) CdZnTe. This material showed clear terracing with Nomarski DIC microscopy (Figure 4.11), but work with image enhancement technology at GEC-Marconi (private communication) had again suggested shallow surface features on each terrace. This material was therefore included in the AFM study.

An AFM scans a fine point across a sample surface with two piezo-electric elements. This 'tip' is in contact with the sample: that is to say, the tip is so close to the sample that the sample exerts a repulsive force on the tip. The tip could conceivably interact with the sample in other ways. The tip is mounted on a cantilever and the deflection of this cantilever is a measure of the contact force. The contact force increases very rapidly as the tip approaches the sample surface: it is a very sensitive indicator of the distance between tip and surface. It is so sensitive that it cannot be used as a measure of surface height except for the flattest of samples. In most cases a feedback loop operates with a third, 'z' piezo which operates to keep the contact force constant. The position of this z-piezo is then a measure of the sample surface height.

The AFM used had a digital feedback loop, with a 14-bit height resolution of either 7.3A over a 12um range, or 1.46A over a 2.4um range. The maximum x-y range was 24 x 24um. At a data acquisition rate of 22kbaud the images were sharp but vibration of the probe caused by transient acceleration at the beginning of each scan line was evident at the edges of some images.

Images were collected with up to 500x500 pixel resolution on a dedicated platform but could be exported to any modern personal computer. Height and also dragging force (the twist of the cantilever) could be acquired on both the forward and reverse sweeps of the probe, because the probe remained in contact with the sample throughout its raster. In general, the reverse sweeps were cleaner because microscopic surface contaminants had been removed by the forward sweep of the probe, much as a gramophone stylus collects fluff. Drift was caused by the adhesive tape used to mount the samples, but this was tolerable.

Software allowed projections of the 3-D data to be constructed from any viewpoint, with colour to represent either height or slope (c.f. Nomarski DIC). Images could be 'levelled' by the subtraction of a plane of best fit or a second-order surface of positive (dome) or negative (saddle) curvature; or each scan line could be levelled by the subtraction of a low-order (1-6) polynomial approximation. This last was found to be most appropriate for the observation of material D. Techniques such as Fourier transform smoothing and edge enhancement techniques were not applied, for fear of creating artefacts.

Materials 'B', 'C' and 'D' were examined with the AFM. Material 'B' is shown in Figures 4.12-4.13; material 'C' is shown in Figures 4.14-4.15; material 'D' is shown in Figures 4.16-4.17.

3.6 Transmission Electron Microscopy

3.6.1 Aims

Transmission electron microscopy (TEM) was thought to be an appropriate technique for the observation of defects in CMT and CdTe layers. It is one of the few techniques that allows the direct observation and characterisation of defects, provided that a thin section of material can be prepared with the introduction of no artefacts.

The investigation of hillocks on CMT was intended to be a minor piece of work. Instead, it produced many interesting results (see preceding chapters). Hillock density depended on substrate pre-treatment - i.e., the formation of a buffer layer - and the buffer layers which performed differently had obviously different surface morphologies, but there was no obvious mechanistic link between this surface morphology and hillock density on a subsequent CMT layer.

This result, supported by etching and Nomarski microscopy (previous chapters) suggested that the hillocks were not merely growth-surface instabilities but crystallographic defects. These could be initiated at crystallographic defects in the buffer layers which need not be visible in surface topography by AFM, and which are likely to be below the resolution of Nomarski DIC on cleaved cross-sections. Perhaps AFM of a cross-section would in future be profitable, though the examination of a specific area of a sample was difficult in the apparatus at our disposal. The buffer layer in this system was where most of the relaxation was thought to take place. It was therefore expected to be defective. With the results from the observations of hillocks, it therefore became a priority to observe the buffer layers of materials 'B' and 'C' in TEM.

3.6.2 Sample Preparation

3.6.2.1 General

CdTe is soft and brittle. TEM requires a sample which is very thin (about 100nm) and undamaged. To see how defect distribution depends on depth, a sample would ideally be viewed in cross-section.

TEM samples are most frequently discs of a standard size, often about 3mm in diameter. By chemical or ion-beam etching, both methods which exert negligible force on the sample, the centre is made very thin, while the edge remains thick to provide strength.

To observe a layer in cross-section, it is first made into a 'sandwich' between inert packing materials, of sufficient thickness that a cylinder of the diameter of a TEM disc may be cut from it. Discs are cut from the end of this cylinder, and the layer normal then lies in the plane of each disc.

This technique was adapted for CMT. It was found that a simple sandwich of two CdTe/GaAs wafers face-to-face with silicon packing was not strong enough. A second, perpendicular packing was also tried. Eventually, external support was tried, in the form of a 'grid' of copper-beryllium alloy, a disc with a single 2mm x 1mm

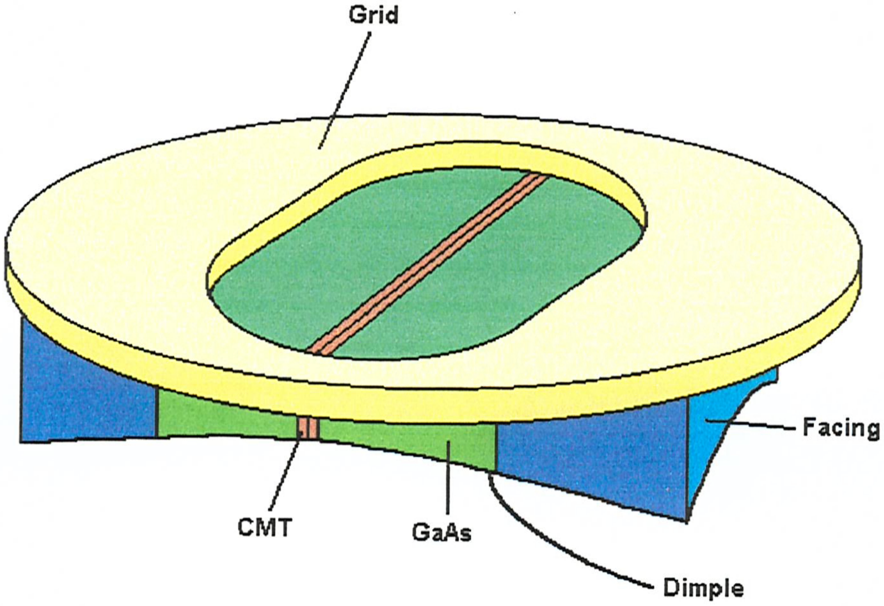

Figure 3.2: Diagram of a TEM foil prepared by the present author.

slot in the centre, glued to one face of the sample with epoxy to support the edges.

It was found to be difficult to etch the side of the layer facing the disc after mounting with ion-beams due to shadowing effects. This was solved by a two-stage 'clean and safe' procedure:

1. Make a sandwich 2mm thick. This is approximately equal to the side of a square with diagonal equal to 3mm diameter of a TEM foil.
2. Cut a 2mm x 2mm rod from this.
3. Cut squares from the end of the rod, 250um thick.
4. Check that the diagonal of the rod does not exceed the 3mm diameter of a TEM foil. If it does, grind the edges on fine emery paper.
5. Polish and ion-beam etch (Ar^+) one side of this square of material. The sample is mounted on the ion-beam etcher with wax by its other face. This makes one 'clean' surface.
6. Glue a grid to this face. This makes the surface 'safe' from further contamination.
7. Now dismount the sample from the ion-beam etcher.
8. Polish and etch the other side until it is electron-transparent.

3.6.2.2 Specifics

TEM foils (Figure 3.2) were made from material 'C' as follows:

1. The wafer was broken along natural cleavage planes by the application of light pressure across the edge of a microscope slide to produce two bars each of approximate width 2mm. The wafer was scribed with a diamond point near the edge to help initiate each fracture.

2. Two pieces of 0.6mm silicon wafer of approximately the same dimensions as the CMT were prepared.

3. The four bars were glued face-to-face with Araldite epoxy resin. The order of assembly was Si-CdTe-CdTe-Si. The two CdTe bars were placed with the CdTe faces touching and the substrates outermost. Epoxy was chosen for its inertness, thermal stability, low contraction during cure and low out-gassing in the vacuum of a TEM. Inertness was necessary as the sample would be exposed to other chemicals (mounting waxes and their solvents). Thermal stability made the joints stable in a focussed electron beam and allowed samples mounted with a suitable low-melting point wax to be removed with moderate heat instead of solvents. Low contraction was essential so as not to cause dislocation motion in the layers. Finally, the high vacuum of a TEM must never be contaminated with organic vapours if the instrument is to function correctly.

4. The glue was left to set overnight.

5. If the diagonal of the assembled rod exceeded 3mm, the edges of the rod were ground on emery paper to reduce the diagonal.

6. The assembled rod was sectioned with a 1" diameter by 200um thick diamond grit blade at 0.15ms^{-1} edge speed under 0.45N load. The cuts were parallel to each other and perpendicular to the wafers. A water-based emulsion cutting fluid (Struers) was used as lubricant. The cut angle was chosen to produce rectangles of diagonal close to but not exceeding 3mm. The rod was held immersed in a bath of cutting fluid with a low melting point wax.

7. Each square was rinsed in a solvent which did not attack the epoxy.

8. The diamond saw was expected to cause much surface damage. Also, sections were limited by their brittleness to 200um thickness, which is too thick for thinning by

ion-beams because of the low material removal rate of this process. The volume of material removed by ion-beam thinning varies as the cube of the thickness removed, because a cone of material is removed. So a mechanical 'pre-thinning' treatment was used, termed 'dimpling': the sample, mounted with wax, rotates under a low load beneath a small brass wheel carrying an abrasive slurry until a 'dimple' of the required depth is produced.

First, one face of the sample was ground with a ½" diameter by 2mm thick brass wheel carrying 6um diamond paste. The sample was mounted on a rotating stage with a low melting point alcohol-soluble wax. The mounting wax had to fulfil certain conditions. It had to have a low melting point, and needed to be completely soluble in a solvent which did not degrade the epoxy. 0.4N load was applied with $0.075ms^{-1}$ wheel circumferential speed. 50um of material was removed.

9. The wheel and mounted sample were rinsed with excess water and a further 25um of material was removed with 1um diamond paste.

10. The wheel and sample were again rinsed and the sample was polished for 5 minutes with a highly viscous mixture of 50nm alumina and propylene glycol. Propylene glycol was chosen because it was viscous, inert to the epoxy, and evaporated very slowly.

11. The sample stage was rinsed, and heated to melt the wax. The sample was removed and quickly bonded to the face of a copper pin designed for the ion-beam thinner, using the same wax. This pin was designed to cool the sample during milling, and hence reduce the milling damage, more effectively than a conventional edge support, even one which was nitrogen cooled.

12. The face of the sample was milled in an Ar^+ ion-beam thinner (Gatan 'PIPS') at 4.2kV accelerating voltage and 7° incident angle for 1 hour with 3 rpm rotation speed. The slightness of the incident angle was limited by the thickness of the edge of the sample over the centre after dimpling. The thicker the edge, the stronger the sample. A 7° incident angle was found to be a reasonable minimum. Of the many samples prepared, those milled in the vicinity of 4.2kV accelerating voltage appeared the most uniformly thin and transparent in the electron microscope.

13. A 'grid' of Cu-Be alloy, being a disc of 3mm diameter with a central oval hole 1mm x 2mm, was bonded with Araldite to the sample face. The glue was allowed to cure overnight.

14. The sample was ground as in stages 8-10. The thicknesses removed were adjusted to leave about 75um of sample at the centre. This thickness was chosen to be as great as possible without necessitating an overly long time (possibly days) to mill to transparency.

15. It was not necessary to remove any residual wax from the second face of the sample; the wax, being hard and brittle at room temperature, could easily be ground away by the dimpling machine.

16. The sample was rinsed in excess alcohol to remove wax from the surface.

17. The sample was milled as in section 12 until a hole visible to the naked eye was produced.

18. The pin was heated, and the sample was removed and cleaned in excess alcohol.

19. The sample was dried thoroughly and mounted in a single-tilt TEM specimen holder with the tilt axis parallel to the original wafer normal; that is, perpendicular to the Araldite glue lines.

Figure 4.18 is a (110) electron diffraction pattern from the sample. This was indexed as in Figure 4.19.

Low-magnification bright-field images with (110) incident beam were taken of a thick region of a sample (Figure 4.20), a thin region (Figure 4.21) and a region with fringes (Figure 4.22).

A higher magnification image near the heterointerface was taken with (110) illumination and an aperture about the (000) and (111) beams.

Finally, a very low magnification image was taken (Figure 4.25).

3.6.3 Plan-view TEM

Material 'E' was a heterostructure of CMT on CdTe on GaAs whose composition and conduction type varied as a function of depth. GEC-Marconi had performed a chemical defect etch on a bevelled sample of this material, and this had shown a non-uniform etch-pit density. The question was posed: what crystallographic defect was associated with each etch pit? The density of etch pits suggested that these defects would be few in number in the visible portion of an ideal TEM sample. A cross-sectional sample would increase this difficulty: the area revealed at each depth would be small. Also, a cross-sectional sample would not intersect 'threading' dislocations normal to a layer, which are those most likely to appear at the surface of a bevelled sample. The logical solution was to take the surface of a bevelled layer as one 'clean', prepared surface of a TEM foil, and then to grind/mill away the back face to transparency, thereby isolating a section of the layer at known depth in plan-view.

A sample of material 'E' was prepared for in-plane TEM as follows:

1. A single bar of width 2mm was cleaved as above.

2. This was bevel-etched as above to reveal surface at all depths in the CMT.

3. This bevel was then cleaved as above into squares with diagonal close to but not exceeding 3mm.

4. A grid was glued to the face of each square, as above.

5. The substrate side of each square was then ground and ion-beam milled to transparency as above.

6. Each square was mounted in a single-tilt TEM specimen holder.

The n^+, high-Cd region of the sample was examined in bright-field with near-001 incident beam (Figure 4.26).

The n^-, low-Cd region of the sample was examined in bright-field with various incident beam directions (Figures 4.27 and 4.28). A (001) diffraction pattern was obtained (Figure 4.29) and indexed (Figure 4.30). With (001) incident beam, a (200) dark-field image was obtained (Figure 4.31).

The p-type, high-Cd region and the CdTe buffer layer were examined in the same way as the n^+, high-Cd region (above); the results are shown in Figures 4.32 and 4.33 respectively.

A (110) electron diffraction pattern of the CdTe buffer layer was obtained (Figure 4.34) and indexed (Figure 4.35).

4. RESULTS

4.1 Studies of Hillocks in MOVPE CMT Layers grown on CdTe Buffer Layers on GaAs

The following are micrographs of hillocks, showing how the various techniques used have given some insight into their structure.

Figures 4.1 and 4.2 are of the same area of material 'A', CMT on 2^{o}-off (001) towards (110) GaAs, the first being taken without Nomarski Differential Interference Contrast (DIC), the second with. With Nomarski contrast, the colours represent slope and this second image reveals the slopes of the facets of the hillocks.

Figure 4.3 shows a cleaved cross-section of a hillock with Nomarski contrast. The photograph confirms that the hillock is raised, and suggests some internal structure. It also suggests that the hillock tapers to a point or a line at either the substrate or the buffer layer.

Figures 4.4-4.7 show the results of etching hillocks: in Polisar 2 (Figure 4.4), in Polisar 2 after the hillocks had been rounded off by a bromine-in-methanol etch (Figure 4.5), and in the etch developed by the present author before and after bromine-in-methanol etch (Figures 4.6 and 4.7 respectively). Note the line features revealed on every hillock: all the lines etched by Polisar 2 are parallel, but this is not so for the new etch. Note also faint hillock-shaped features of reversed contrast (i.e., negative relief) in the results from the new etch.

Figure 4.8 shows a reflection synchrotron X-ray topograph of a larger area than any of the optical micrographs 4.1-4.7. The scale is such that the density of black spots is similar to the density of hillocks. The crescent-shaped features corresponded to depressions in the surface.

4.2 Studies of the Topography of LPE CMT and CdTe Buffer Layers on GaAs

Figures 4.9 and 4.10 show scanning electron micrographs (SEM) of CdTe buffer layers on GaAs. Figure 4.9 shows CdTe produced using DIPT precursor. CMT deposited on this buffer layer would have many hillocks. The buffer layer of Figure 4.10 had MATe precursor; CMT deposited on this buffer layer would have few hillocks. Note the poor contrast, indicating low surface relief, and the significant differences between the two structures: the first is isotropic; the second is anisotropic.

Figure 4.11 is an optical micrograph with Nomarski contrast of an LPE layer. Note the broad terraces.

Figures 4.12-13 and 4.14-15 show AFM images of the surfaces seen in Figures 4.9 and 4.10 respectively. Note the differences in scale of the smallest features. Note also that both surfaces now appear anisotropic. All these images have false colour to give the effect of oblique illumination from the right. On Figures 4.14-15 the line features mark the bottoms of trenches.

Figures 4.16-17 show AFM images of the LPE material shown in Figure 4.11. Note the difference in scale. These images are of the flat portion of a terrace between steps. In these two images, the false colour represents height: high areas are pale; low areas are dark. The broad vertical dark/light bands suggesting waviness are an artefact of the image levelling process. Note also the angular feature on the left of Figure 4.16

4.3 Transmission Electron Microscopy of CdTe and CMT

The remainder of the results in this chapter are transmission electron micrographs (TEM), electron diffraction patterns and their indexes. Features of note on all images are:

1. Wavy smeared lines representing dislocations. As the pass through the sample, their contrast changes, giving a 'stripy' effect.

2. Straight lines of lamellar defects viewed edge-on

3. Broad, 'smoky' dark/light bands in the background, indicating bend in the sample.

4. Dark or light diffuse 'halos' surrounding features, indicating associated strain.

5. Fringes: those which are too broad to be atomic planes are 'Moiré' fringes, showing where the electron beam has passed through two different materials.

6. Atomic planes / files: straight lines / regular arrays of dots. Each dot represents a row of lattice points viewed end-on.

The magnification of a TEM may be varied over several orders of magnitude and must be taken into account when interpreting each image.

Figures 4.18-4.25 are of the MATe buffer layer from Figure 4.10 in cross-section. Several samples were used to obtain this set of images. They show the dislocation structure of the layer and the nature of the lamellar defects in it.

The remainder of the images are from a set of foils prepared from a complex CMT/CdTe/GaAs heterostructure, in plan-view. They may be divided into four sets from four distinct regions of the sample:

Figures	Region
4.26	n^+, high Cd CMT
4.27-31	n^-, low Cd CMT
4.32	p-type, high Cd CMT
4.33-35	CdTe

The number of photographs from each region is a measure of the level of interest in that region. The oval features are of note in the n^-, low-Cd region (Figures 4.27-31). They can be viewed edge-on (Figure 4.28), have an orientation relationship with the matrix, and show little strain. They are revealed in (200) dark-field TEM (Figure 4.31). The diffraction pattern of this region (Figure 4.29) and the CdTe (Figure 4.34) show maxima in unusual positions.

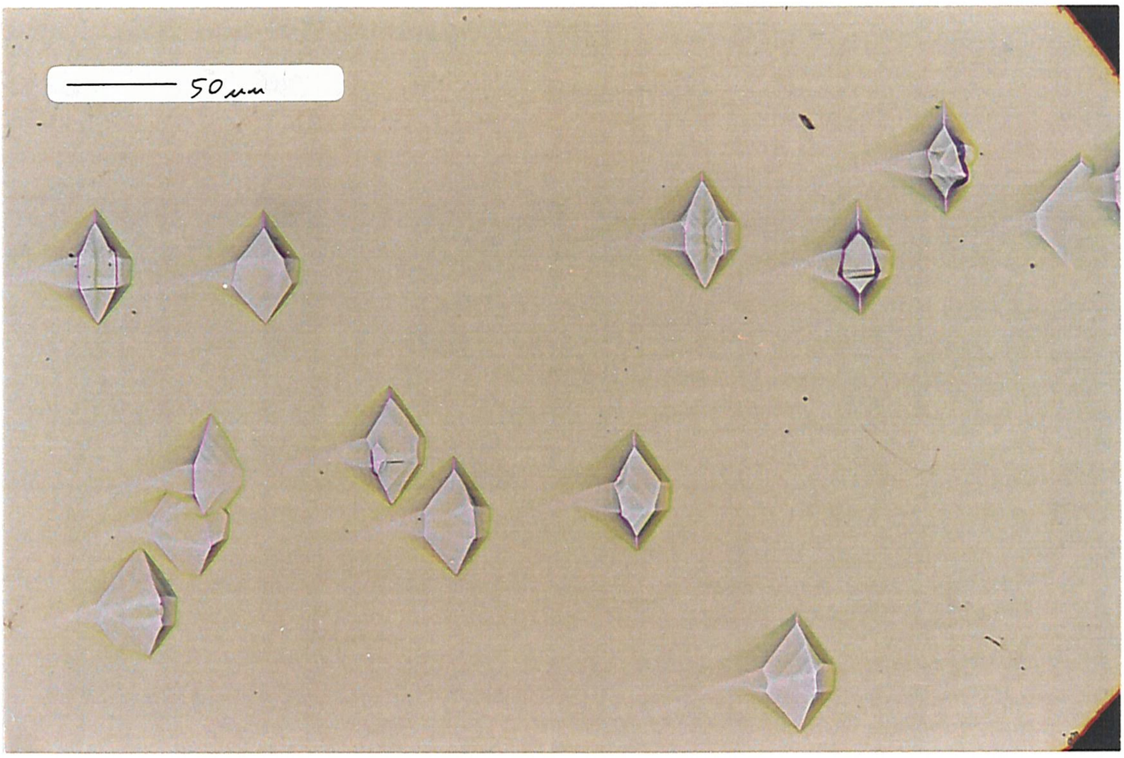

Figure 4.1: Material 'A', optical micrograph

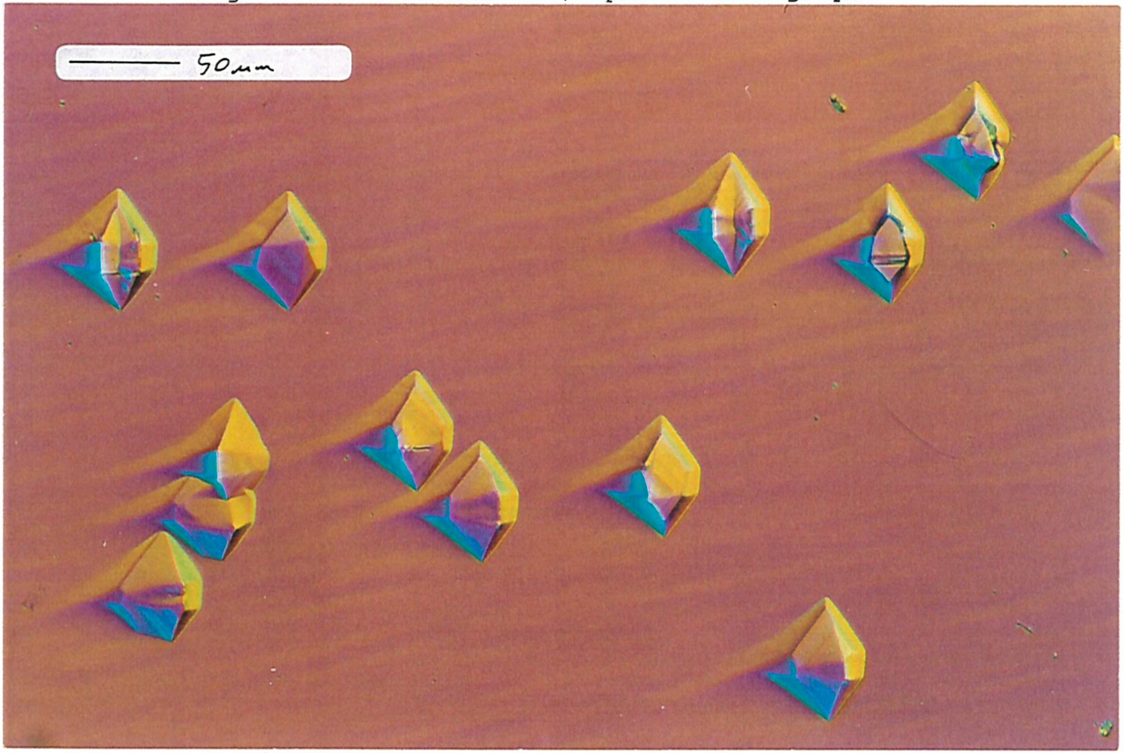

Figure 4.2: Material 'A', Nomarski DIC

Figure 4.3: Material 'A', cross section. Nomarski DIC

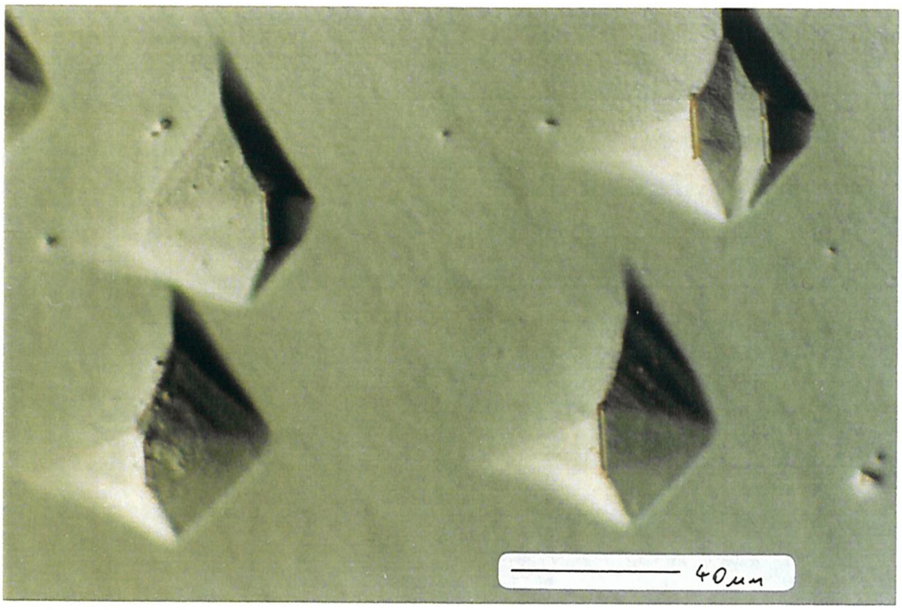

Figure 4.4: Material 'A', after Polisar etch. Nomarski DIC

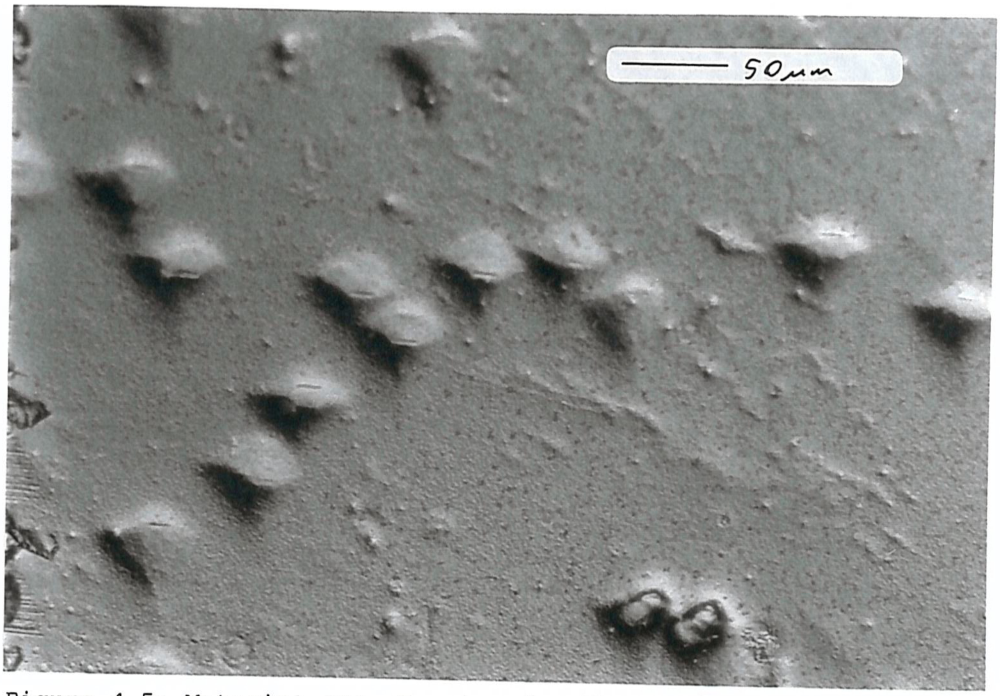

Figure 4.5: Material 'A'. Bromine / methanol then Polisar etch. Nomarski DIC

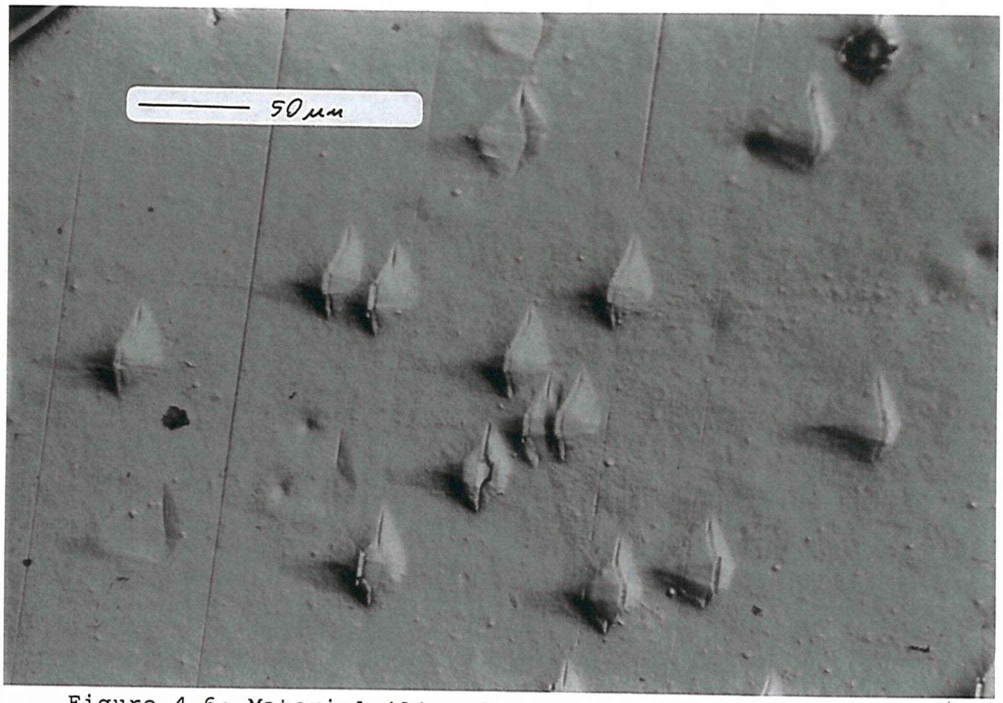

Figure 4.6: Material 'A', after new etch. Nomarski DIC

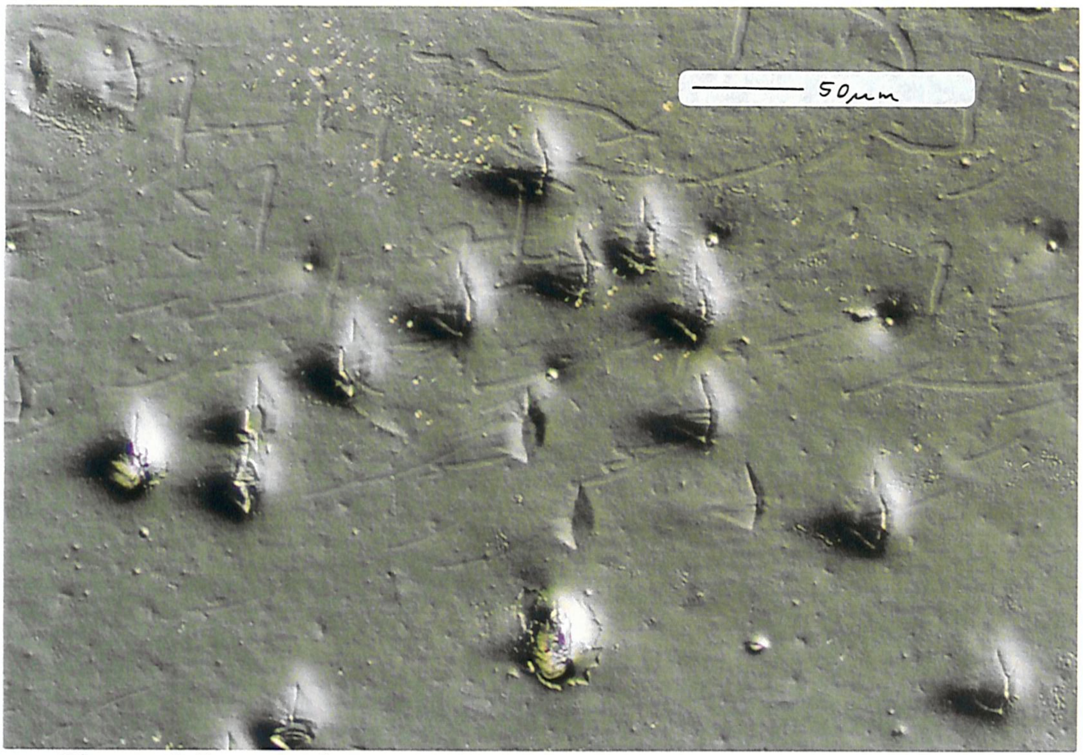

Figure 4.7: Material 'A'; bromine / methanol then new etch.
Nomarski DIC.

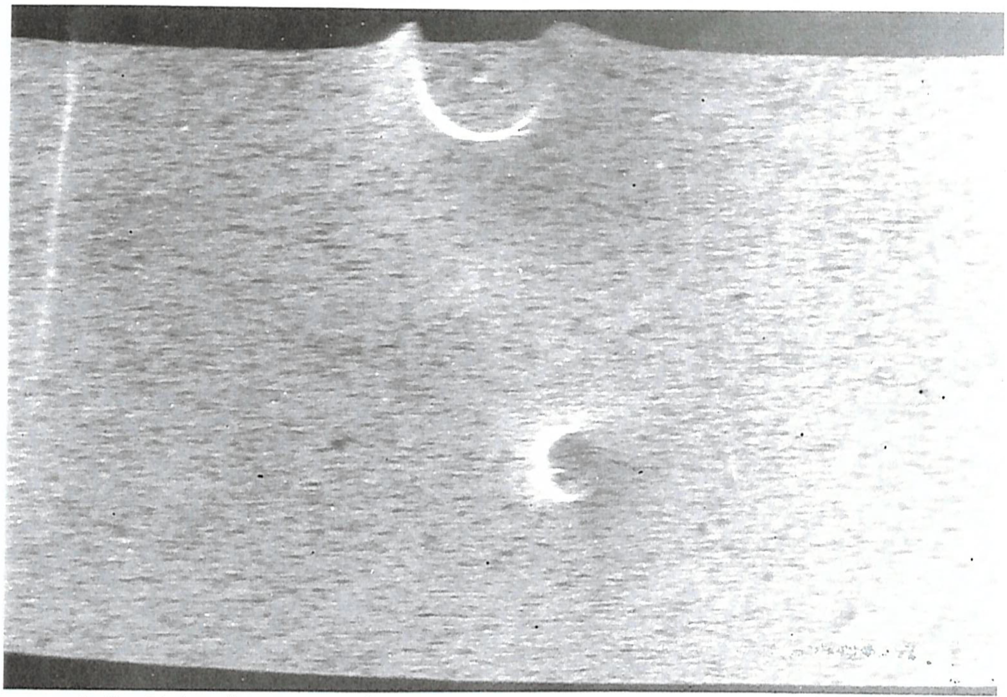

Figure 4.8: Material 'A', (113) reflection synchrotron X-ray topograph

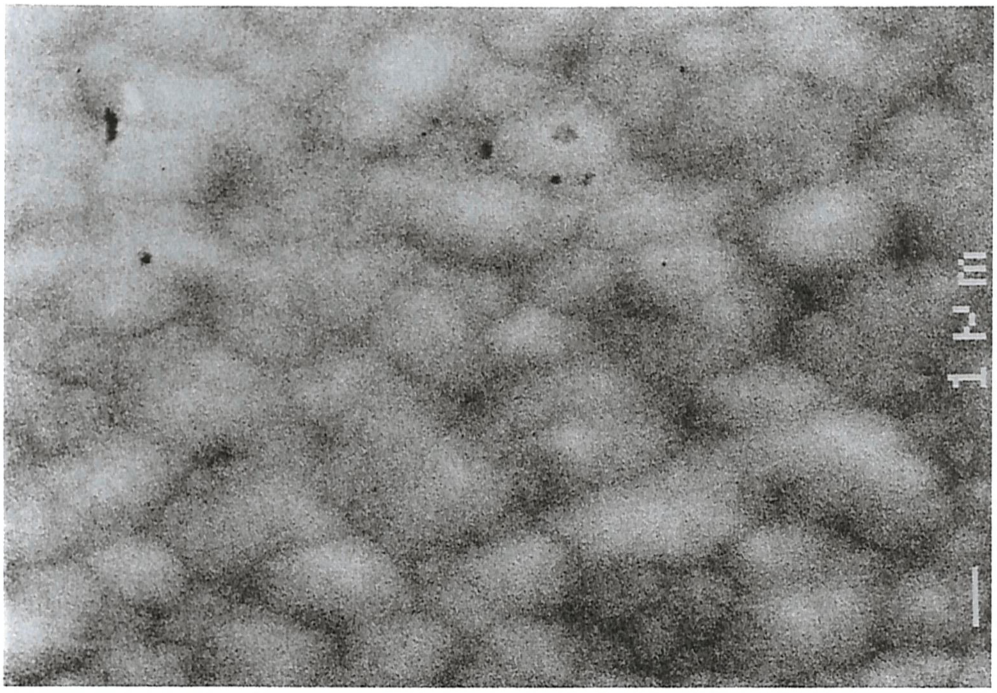

Figure 4.9: Material 'B'. Secondary electron image

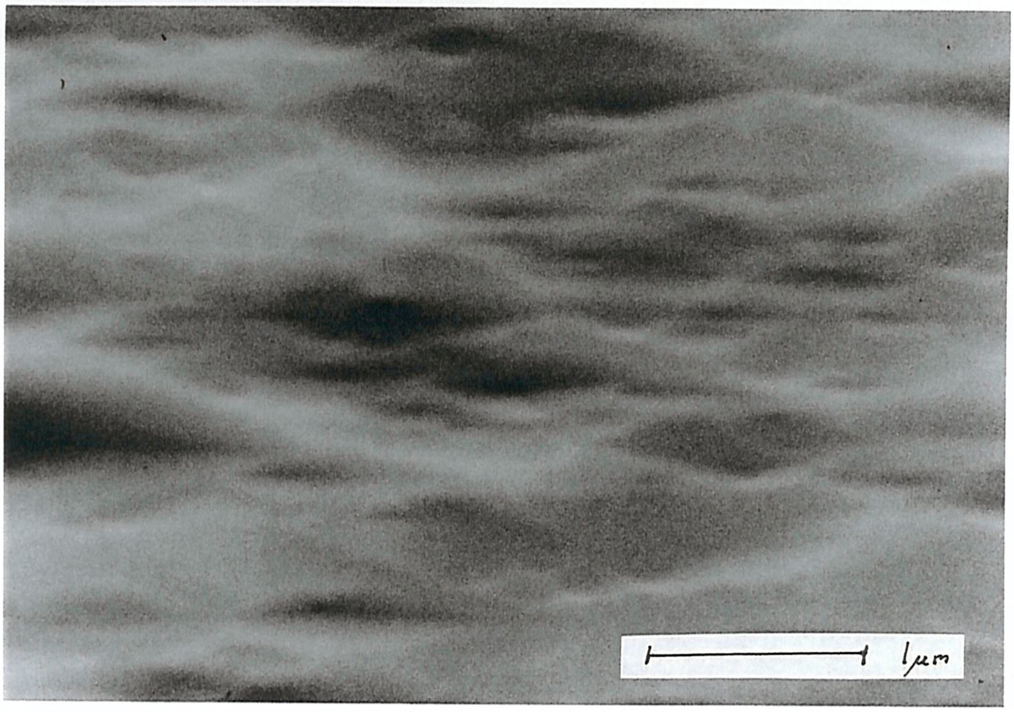

Figure 4.10: Material 'C'. Secondary electron image.

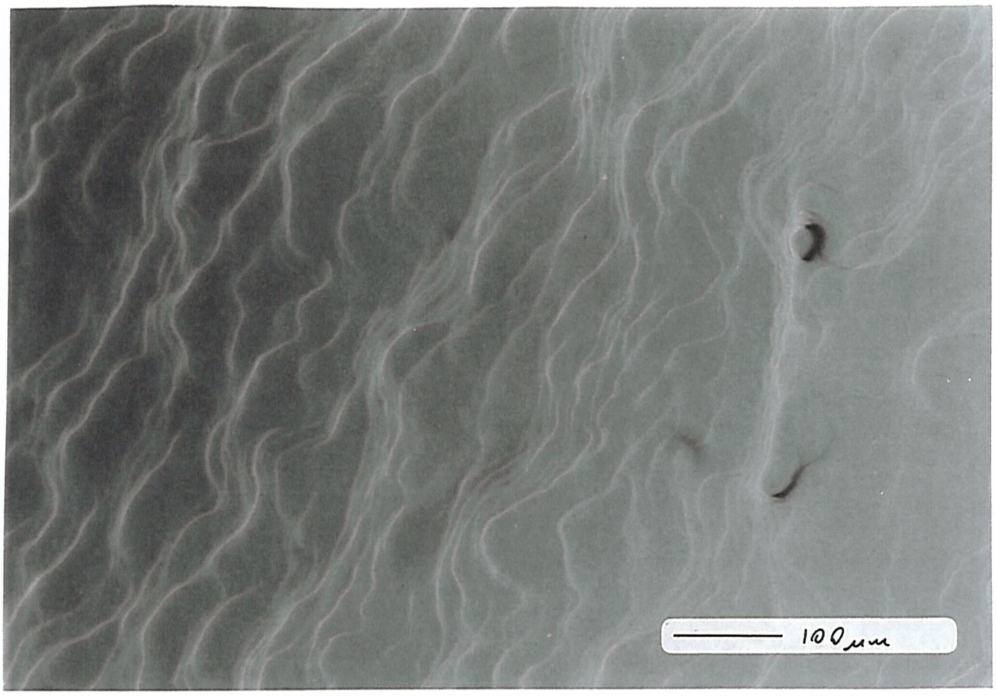

Figure 4.11: Material 'D'. Nomarski DIC

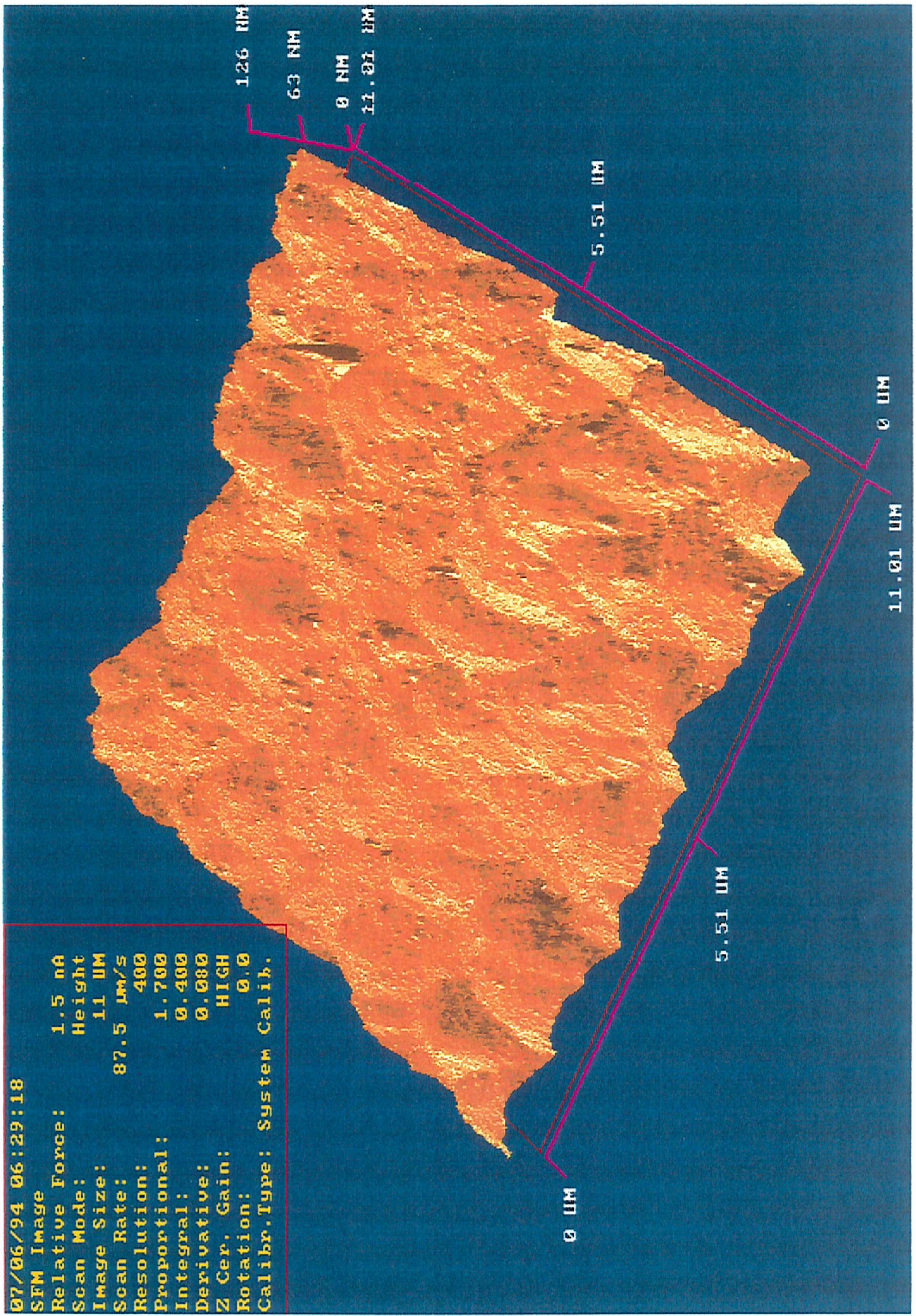

```
07/06/94 06:29:18
SFM Image
Relative Force:       1.5 nA
Scan Mode:            Height
Image Size:            11 UM
Scan Rate:        87.5 µm/s
Resolution:              400
Proportional:          1.700
Integral:              0.400
Derivative:            0.080
Z Cer. Gain:            HIGH
Rotation:                0.0
Calibr.Type: System Calib.
```

Figure 4.12: Material 'B', AFM

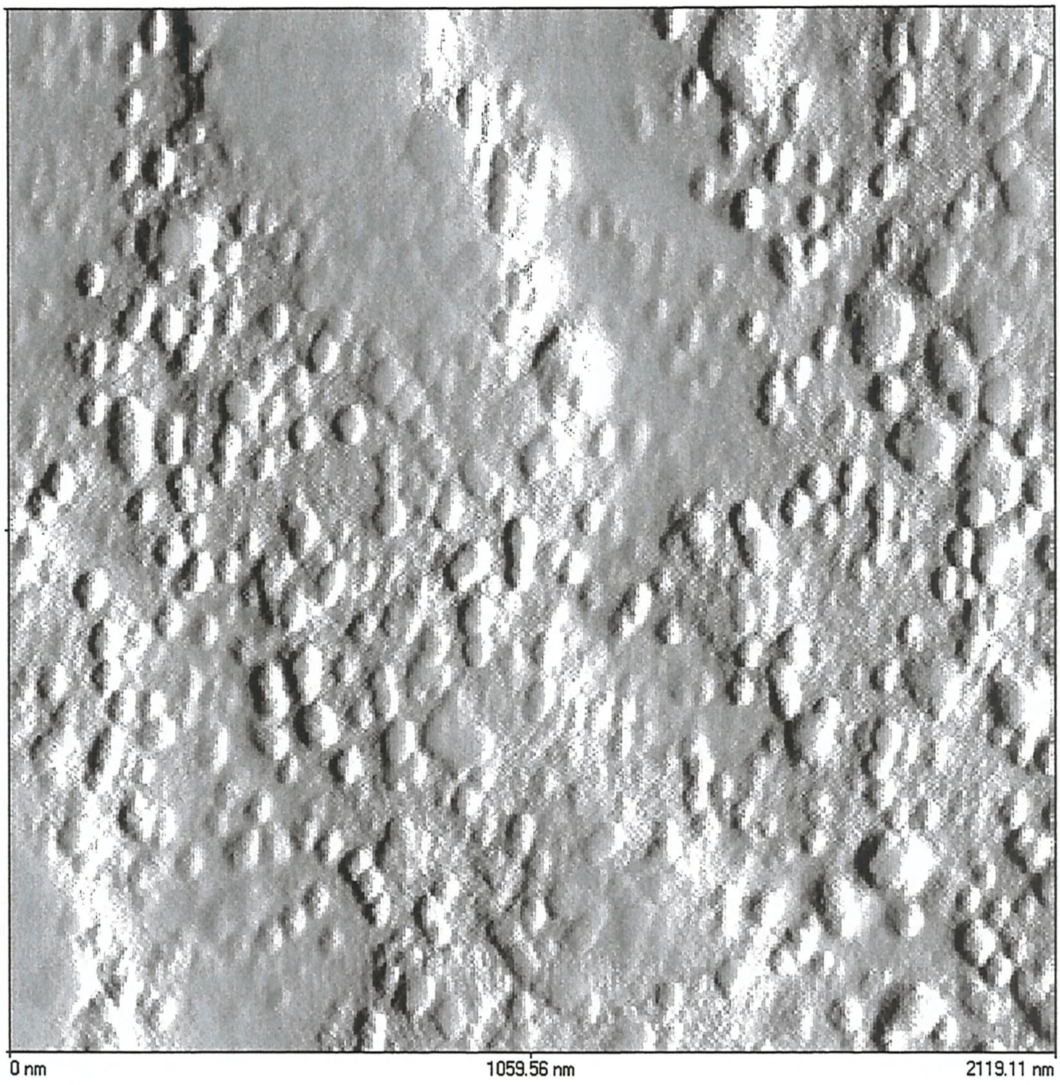

Figure 4.13: Material 'B', AFM

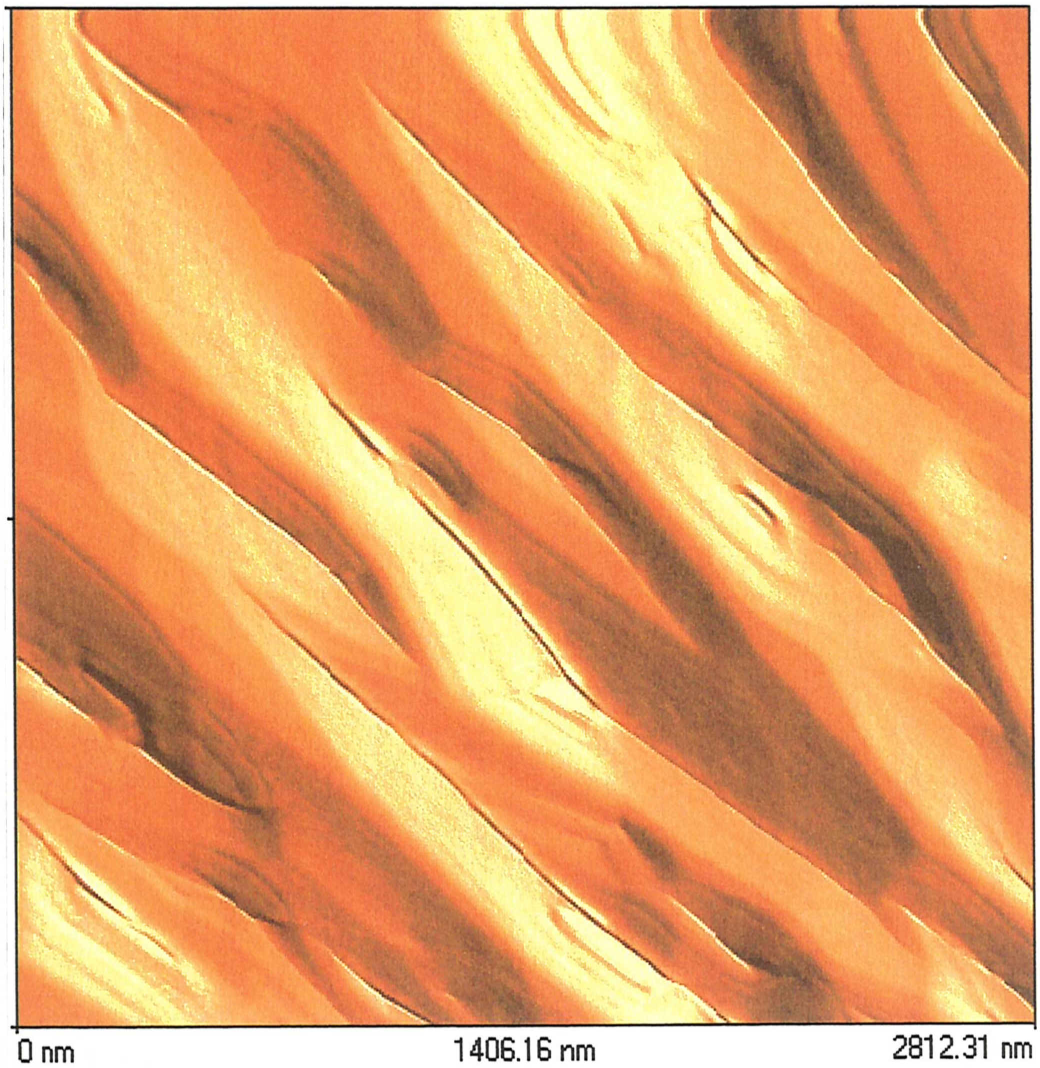

Figure 4.14: Material 'C', AFM

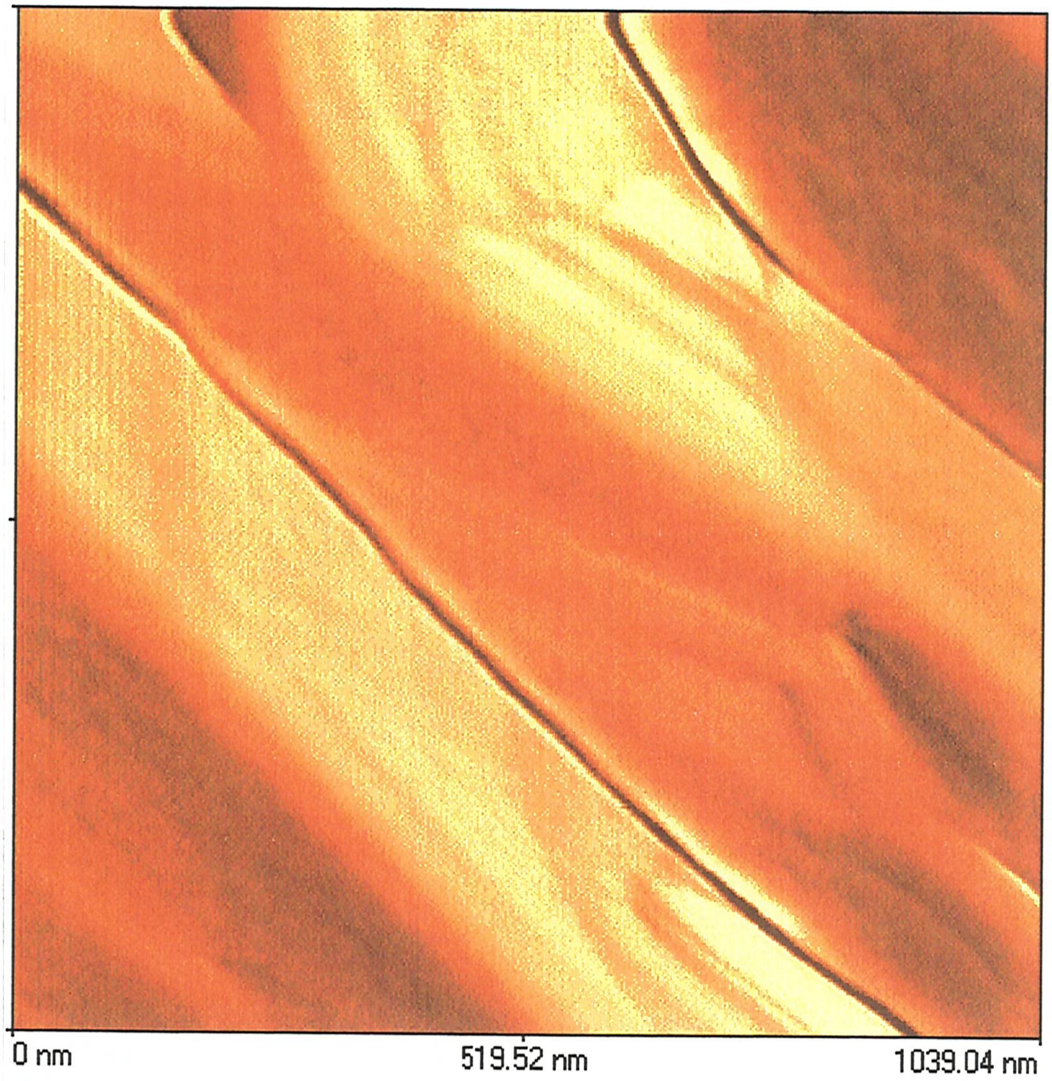

Figure 4.15: Material 'C', AFM

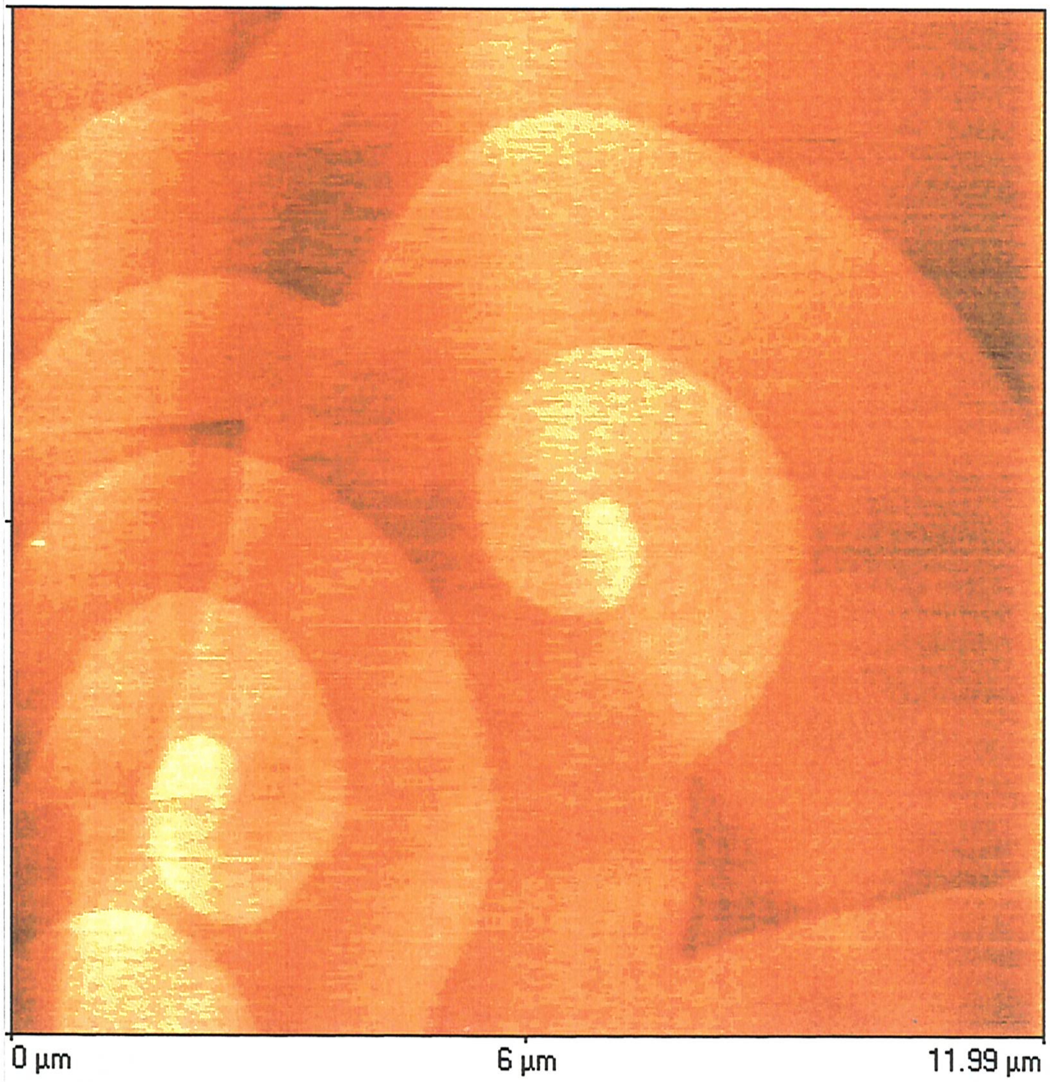

Figure 4.16: Material 'D', AFM

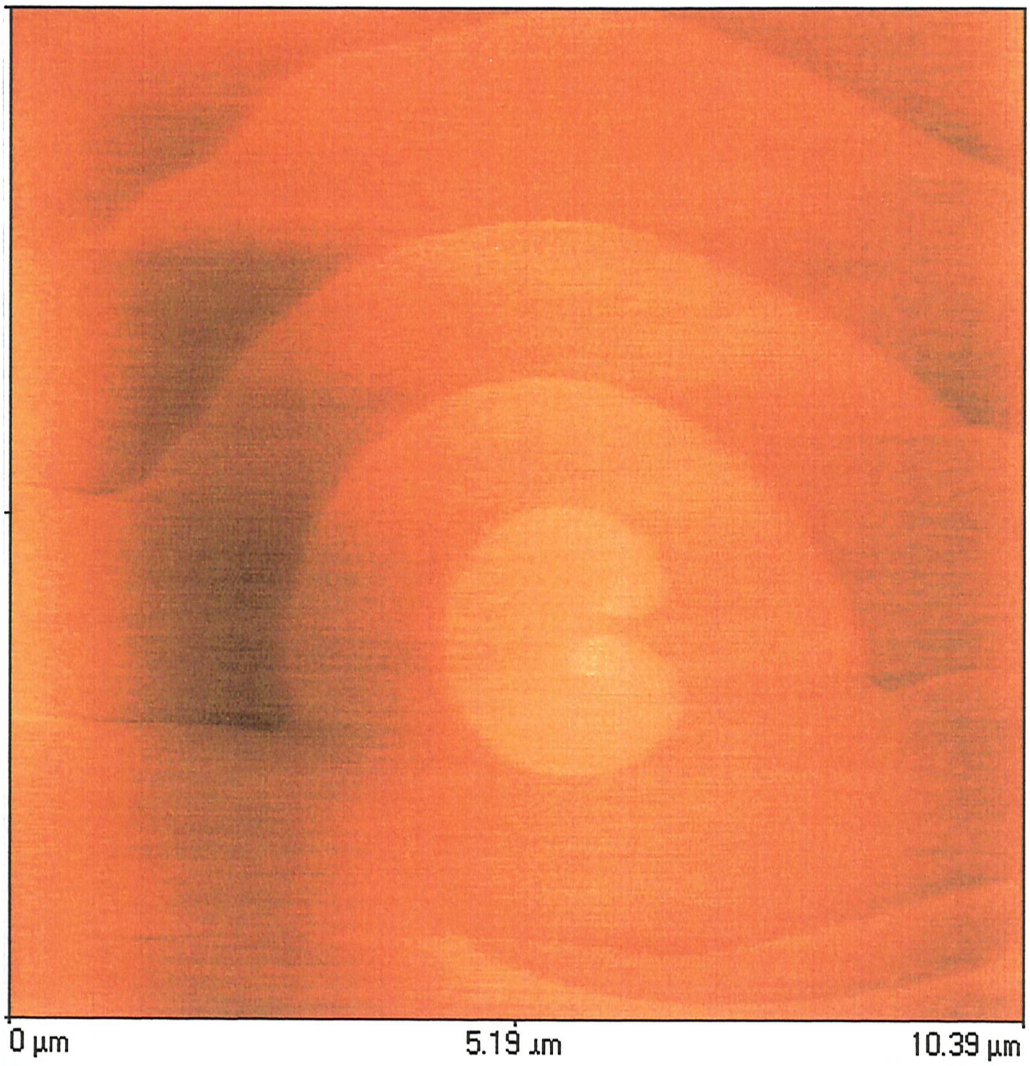

Figure 4.17: Material 'D', AFM

Figure 4.18: Material 'C'. Heterointerface. (110) electron diffraction pattern.

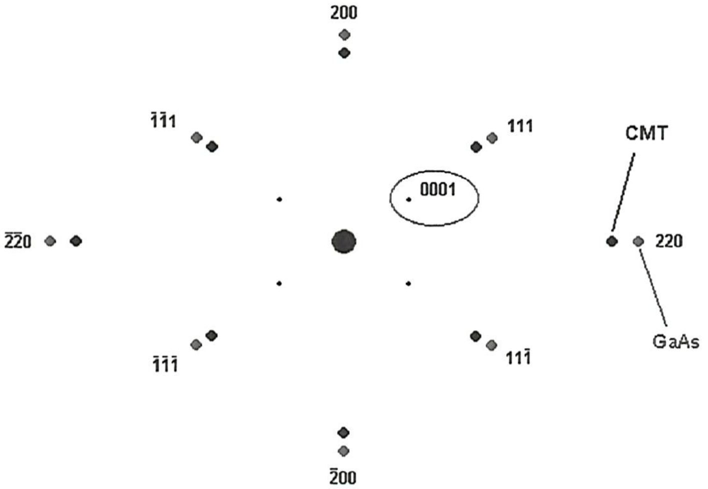

Figure 4.19: Index to Figure 4.18

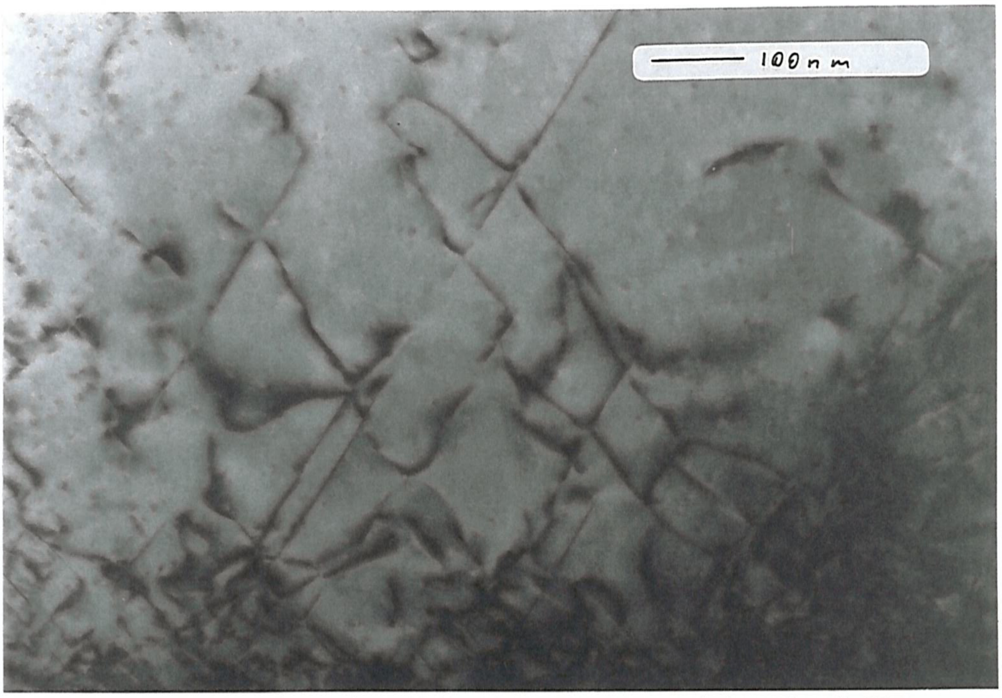

Figure 4.20: Material 'C'. CdTe layer. Bright-field TEM. (110) illumination. Heterointerface at bottom of image.

Figure 4.21: Material 'C'. Bright-field TEM, (110) illumiation.

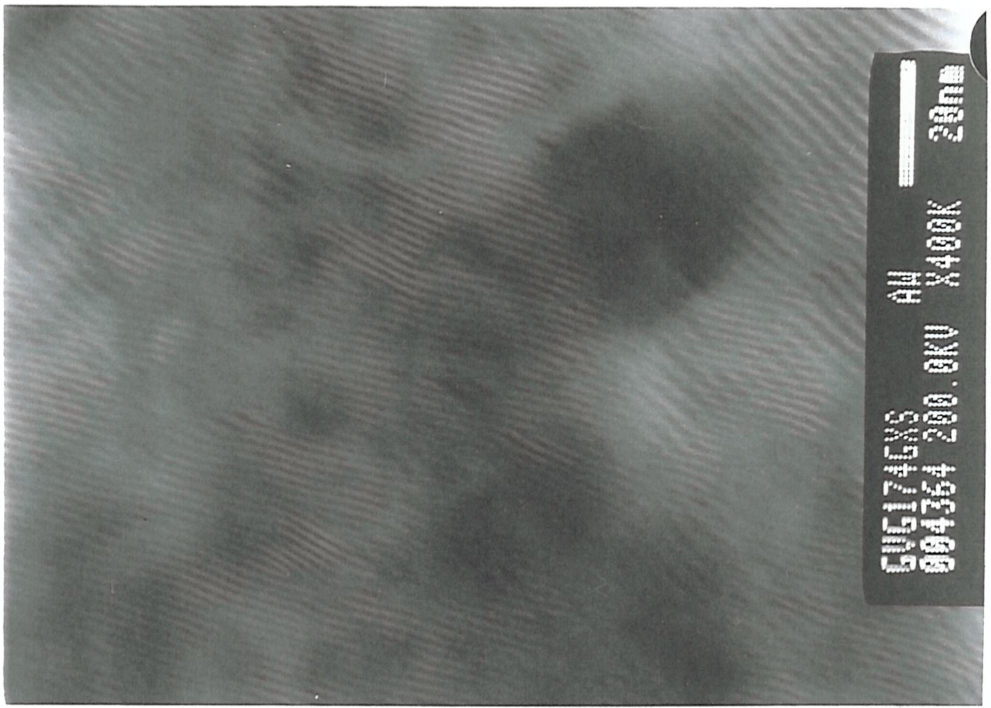

Figure 4.22: Material 'C', bright-field TEM. (110) illumination.

Figure 4.23: Material 'C'. TEM with (000) and (111) diffracted beams. (110) illumination. CdTe layer. Heterointerface at bottom of image.

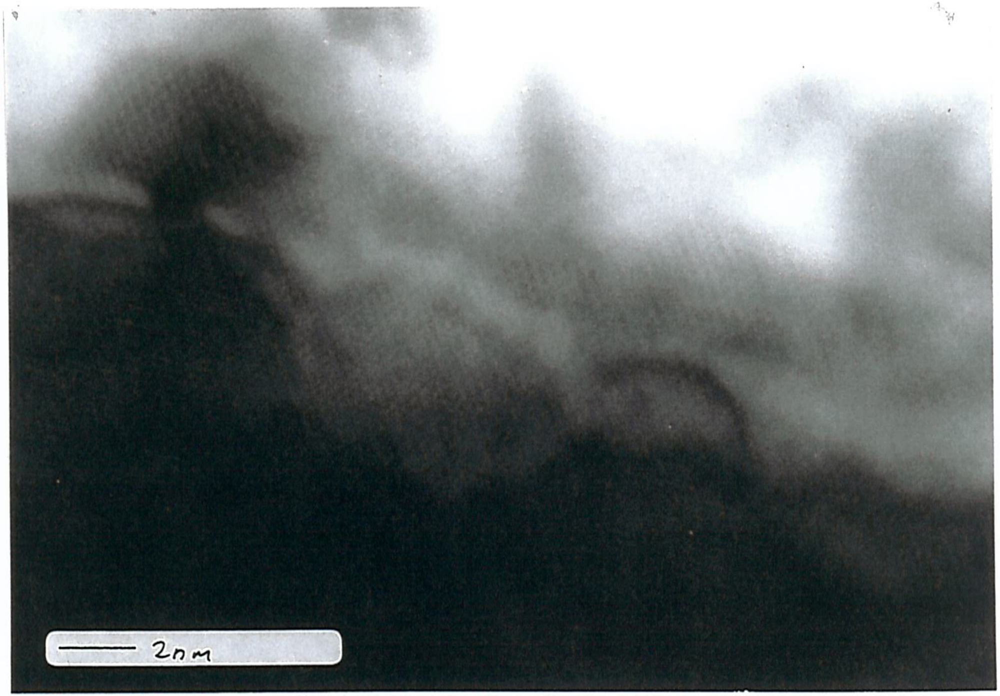

Figure 4.24: Material 'C'.
TEM with (000), (111) and (11$\underline{1}$) diffracted beams. (110) illumiantion

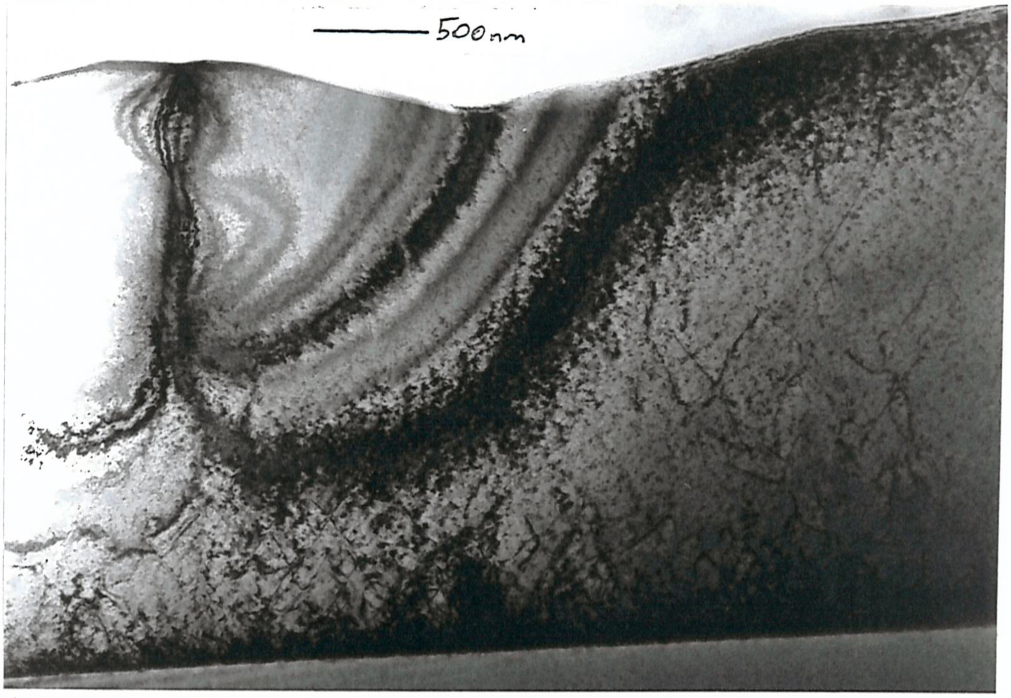

Figure 4.25: Material 'C'. Bright-field TEM, (110) illumination.

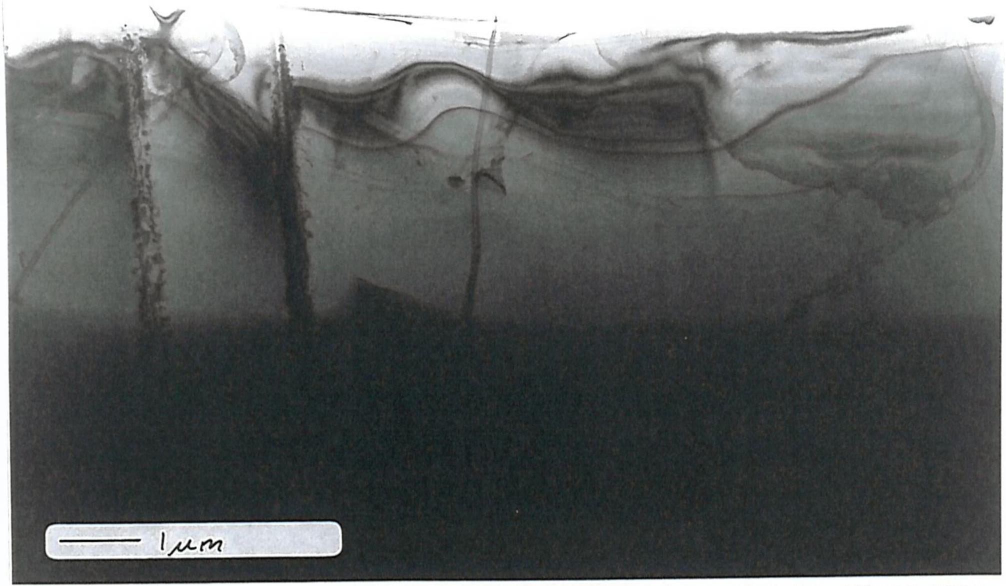

Figure 4.26: Material 'E'. n+, high-Cd region. Bright-field TEM (110) illumination.

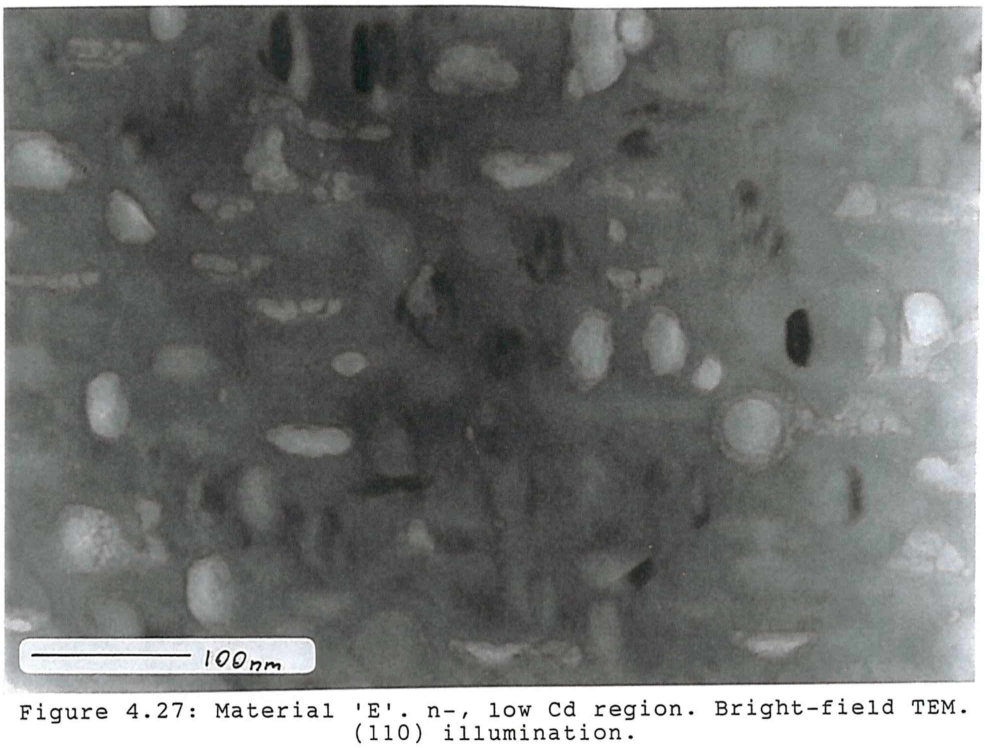

Figure 4.27: Material 'E'. n-, low Cd region. Bright-field TEM. (110) illumination.

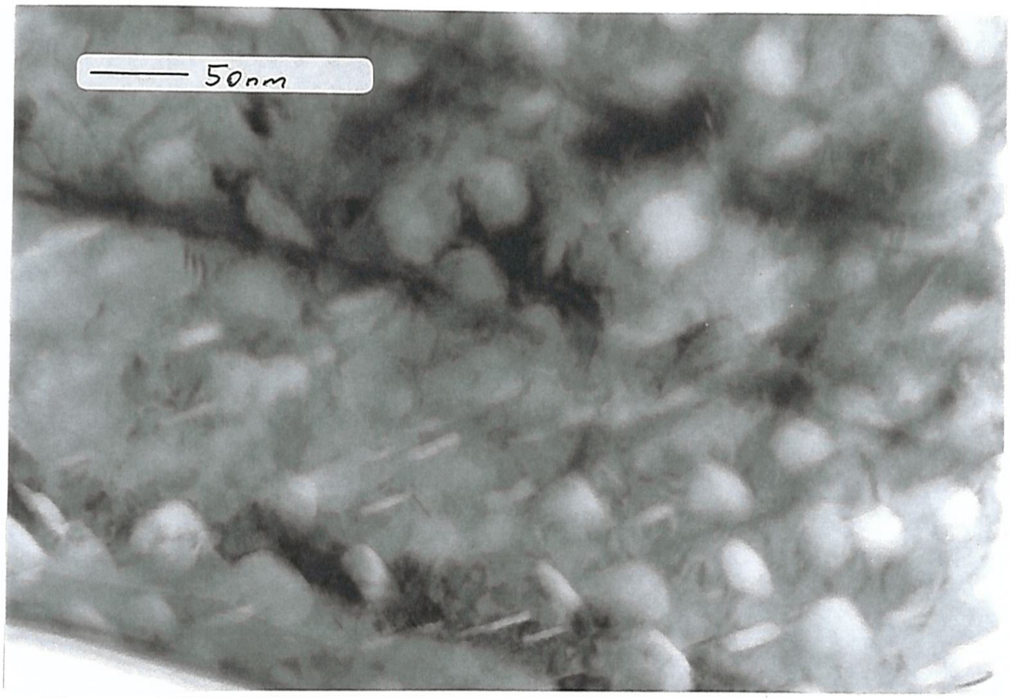

Figure 4.28: Material 'E'. n-, low-Cd region. Bright-field TEM.

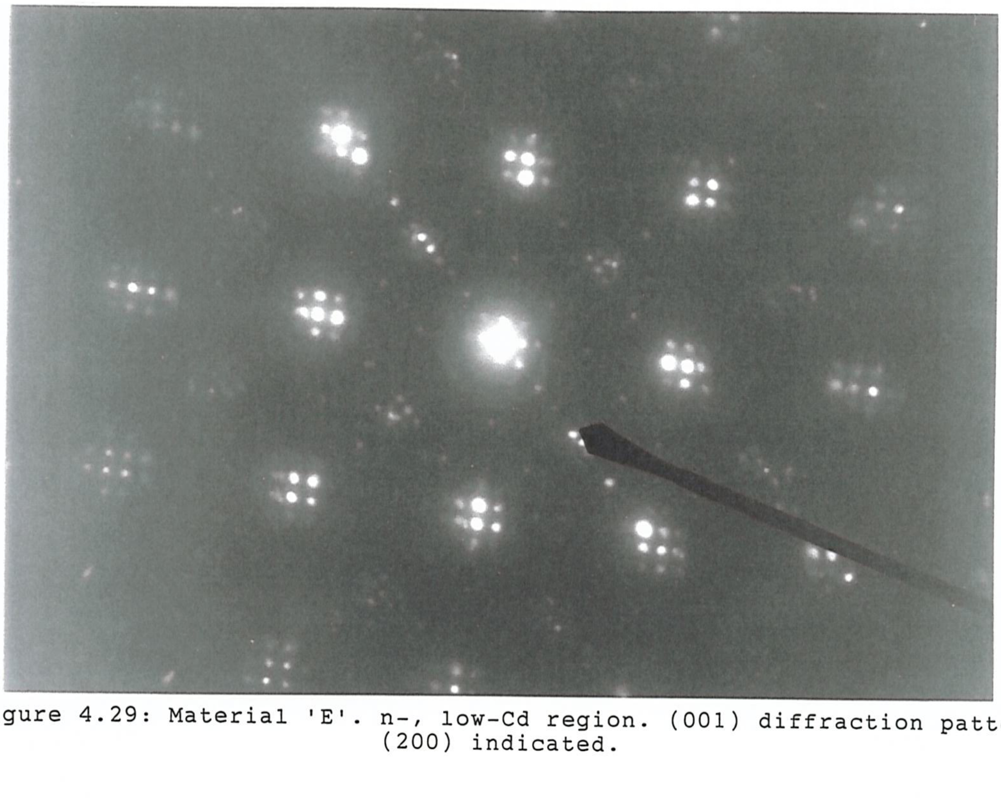

Figure 4.29: Material 'E'. n-, low-Cd region. (001) diffraction pattern. (200) indicated.

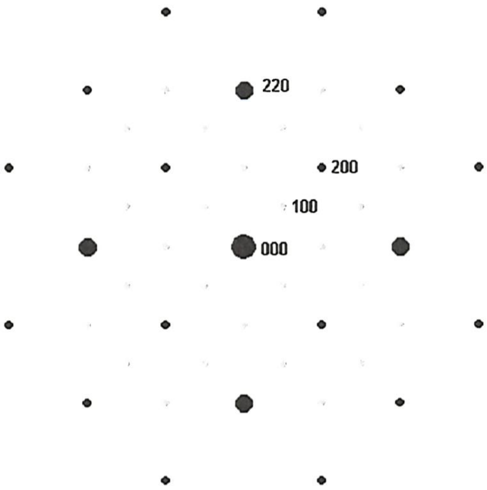

Figure 4.30: Index to Figure 4.29

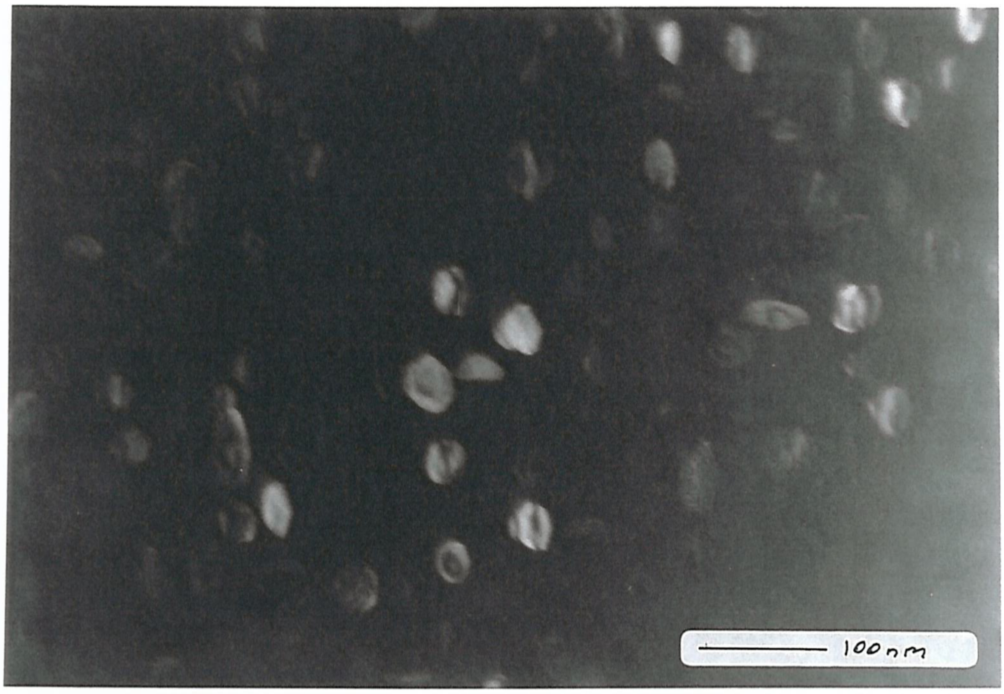

Figure 4.31: Material 'E'. n-, low-Cd region. (200) dark-field TEM. (001) illumination.

Figure 4.32: Material 'E'. p-type, high-Cd region. Bright-field TEM (001) illumination.

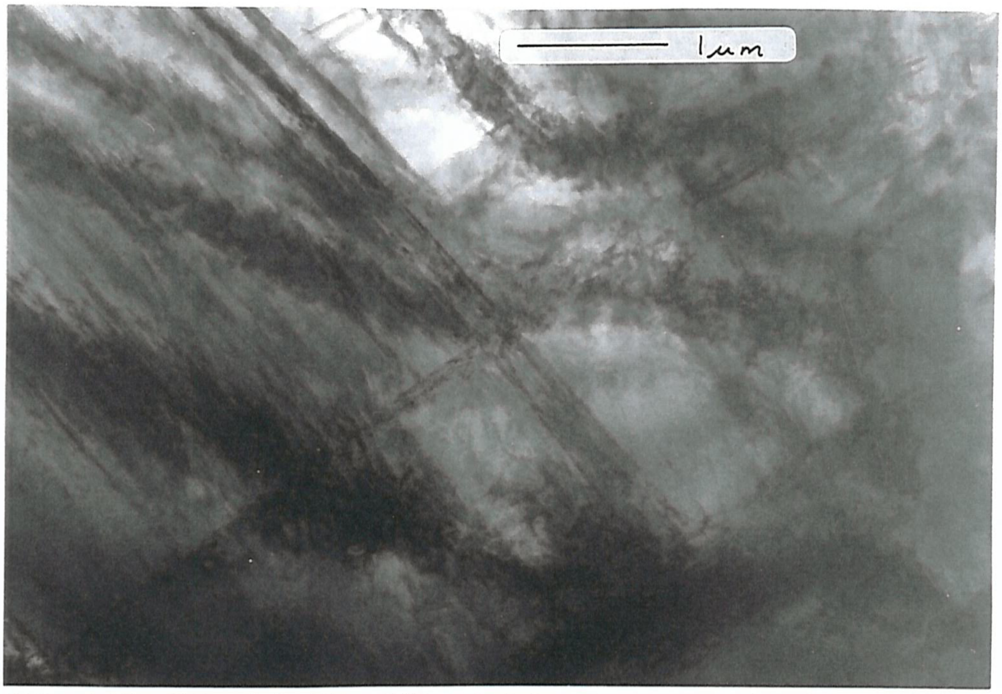

Figure 4.33: Material 'E', CdTe. Bright-firld TEM, (001) illumination.

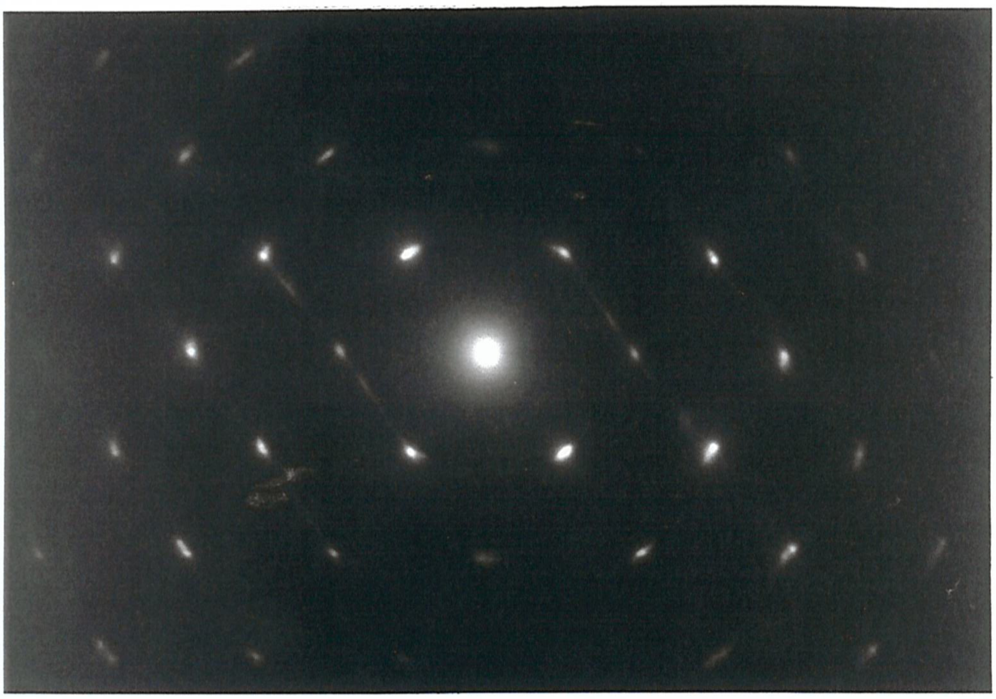

Figure 4.34: Material 'E', CdTe. (110) electron diffraction pattern.

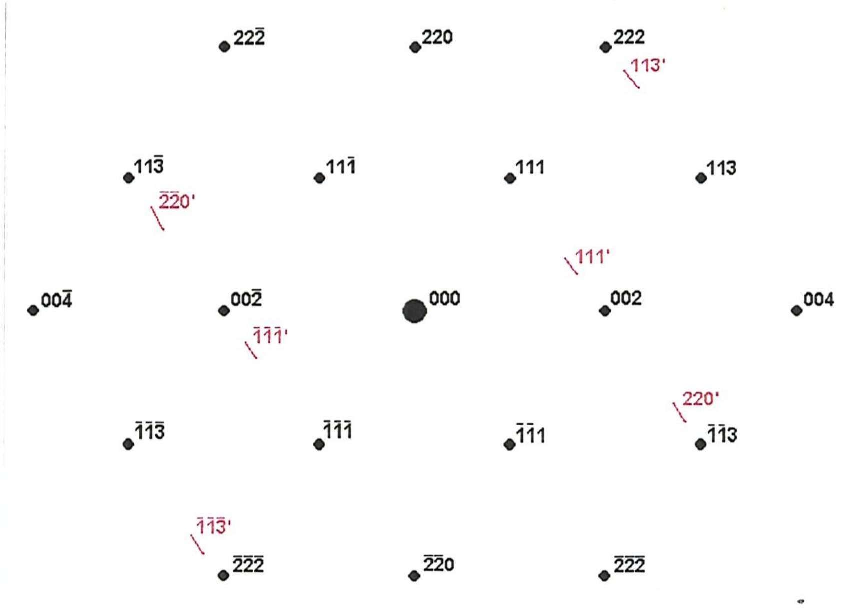

Figure 4.35: Indexing of Figure 4.35

5. Discussion

5.1 On Hillocks

In a Nomarski differential interference contrast (DIC) image, slope variations are shown as colour variations. A Nomarski image of the same area as shown in Figure 4.1 (Figure 4.2) showed that all the hillocks possessed some facets of the same colour and, therefore, slope. The faceting means that the hillocks are crystalline and not amorphous. That they share common facets suggests that they share some orientation relationship, which suggests that their orientation is related to the orientaion of the matrix. Nomarski does not, however, allow the facets to be given Miller indices.

Crack propagation is sensitive to microstructure. A layer of Material A was split along a cleavage plane (as Nouruzi-Khorasani et al. (1990), section 2.3.3), and the new surface was observed with Nomraski DIC. Figure 4.3 shows a hillock cleaved approximately through the centre. The buffer layer and the CMT may easily be distinguished, and their thicknesses may be estimated as 2um and 15um respectively. The hillock seems to be clearly delineated and appears to have internal structure. It appears clearly to meet the CdTe at a line or a point.

5.1.1 Comparison with Previous Observations of Hillocks

Koestner and Schaake (1988) and Million et al. (1988) observed hillocks on (001) surfaces of molecular beam epitaxial (MBE) CMT on GaAs. They suggested that these were composed of one or more twins, and that:

> 'The size being the same for the majority of defects, this indicates that they are not generated during growth but during the first stage of the epitaxy.'

Angelo et al (1994) have observed twins in (001) CdTe layers by TEM, and Cheng et al. (1994) have found an effect of substrate preparation on this system.

Nouruzi-Khorasani et al. (1990) cleaved hillocks and observed some evidence for internal structure. They performed TEM work which suggested that each hillock was composed of many twins.

Koestner et al. (1989) showed that layers grown by Molecular Beam Epitaxy (MBE) on (112) substrates showed very few hillocks. In subsequent work (1991) they observed that they could nucleate hillocks in their apparatus by mercury vapour pressure bursts. They suggested that mercury droplets or clusters could nucleate hillocks. Sporken et al. (1988) claimed they had observed such mercury clusters on MBE CMT surfaces.

It has been found that CdTe can be grown on GaAs with either (111) or (001) parallel to (001). It has been suggested that substrate temperature and surface can influence the orientation (Otsuka et al. (1985), Faurie et al (1986) and Ponce et al. (1986)). In the (111):(001) system, twins can arise by 'double positioning': the two fold symmetry of a perfectly oriented (001) surface means that nuclei must have equally low energy in either of two orientations related by a rotation of 180^{o} about the surface normal. These two orientations are related as rotation twins (see preceding sections). If the growth front is (111), (111) twin boundaries can easily be introduced by a simple stacking error, e.g.:

$$\ldots\ Hg_A\ Te_A\ Hg_B\ Te_B\ Hg_C\ Te_C\ Hg_B\ Te_B\ Hg_A\ Te_A\ \ldots$$

Cibert et al. (1989) suggested that (111) layers of CdTe might contain fewer 'double-positioning' twins if they were deposited on a surface which was not exactly of a low index. This could be because of the reduced symmetry of such a surface.

The growth rate of CdTe is a function of growth orientation. Cinader and Raizman (1992) have written of this:

> 'Considerable changes ... have been found ... the orientational anisotropy of the growth rate leads to hillock formation ... Structural or morphological defects stimulate in the growth process local growth in orientations of higher growth rates.'

These authors suggested the observation of twins by X-ray diffraction. Other authors have explored the technique. Glass and Appleby-Woods (1992) repeatedly etched a (111) layer on sapphire and observed changes in the reflection X-ray diffraction pattern of the surface (estimated to be a layer 1um deep). They found that the concentration of double-positioning twins varied with depth in the layer. Saha et al. (1988) measured the line width of X-ray diffraction maxima from CdTe (111) on glass to determine the density of stacking faults. Iwanaga et al. (1991) have suggested the following methods:

1. (001) is a cleavage plane in CMT. This is equivalent to (411) in a twin, which is not a cleavage plane; so crack paths should deviate in twins.

2. The shapes of etch pits on a surface are sensitive to the index of the surface.

3. The intensities of various diffraction maxima should vary as a function of position in a sample which contains twins.

The authors claimed they observed all these effects.

5.1.2 A possible crystallographic interpretation of optical micrographs of hillocks in the present work.

The hillocks observed in the present work showed facets. Therefore the hillocks were crystalline rather than amorphous, and the facets could reasonably be assumed to be low-order crystallographic planes. The angles of these facets with the surface of the matrix layer were difficult to determine, but the directions in which the facets intersected this (001) surface were easily determined. The expected lines of intersection of low order planes of a twin with (001) may be calculated, and it may thus be seen if the outline of a hillock is consistent with its being a twin, as follows:

A typical hillock shape is shown in Figure 5.1. Symmetry suggests that the twin plane is in the zone $[1\underline{1}0]$. Then the twin plane could be (111), as shown in Figure 5.2.

Let directions in the twin be donated by a "'" suffix.

[111] is parallel to [111]'.

In the cubic system, [hkl] is normal to (hkl).

As described earlier, orientations in the twin may be calculated as follows:

$$\tfrac{1}{3}\begin{pmatrix}\underline{1} & 2 & 2\\ 2 & \underline{1} & 2\\ 2 & 2 & \underline{1}\end{pmatrix}\begin{pmatrix}h\\ k\\ l\end{pmatrix} = (hkl)'$$

Because this matrix represents a rotation by 180°, it obviously equals its own inverse.

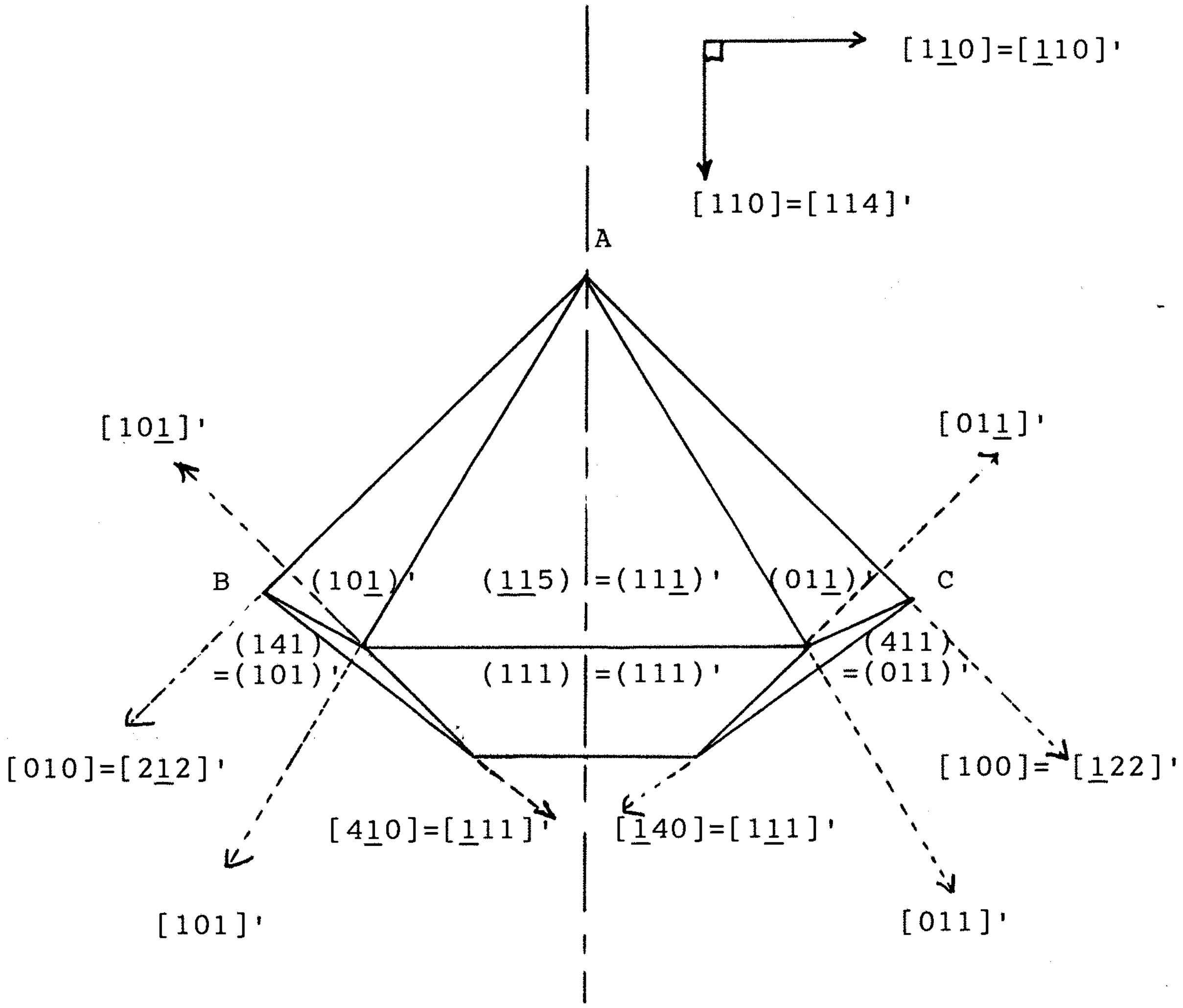

Figure 5.1: Theory proposed by the present author for the crystallographic structure of a hillock on the surface of (001) CMT.

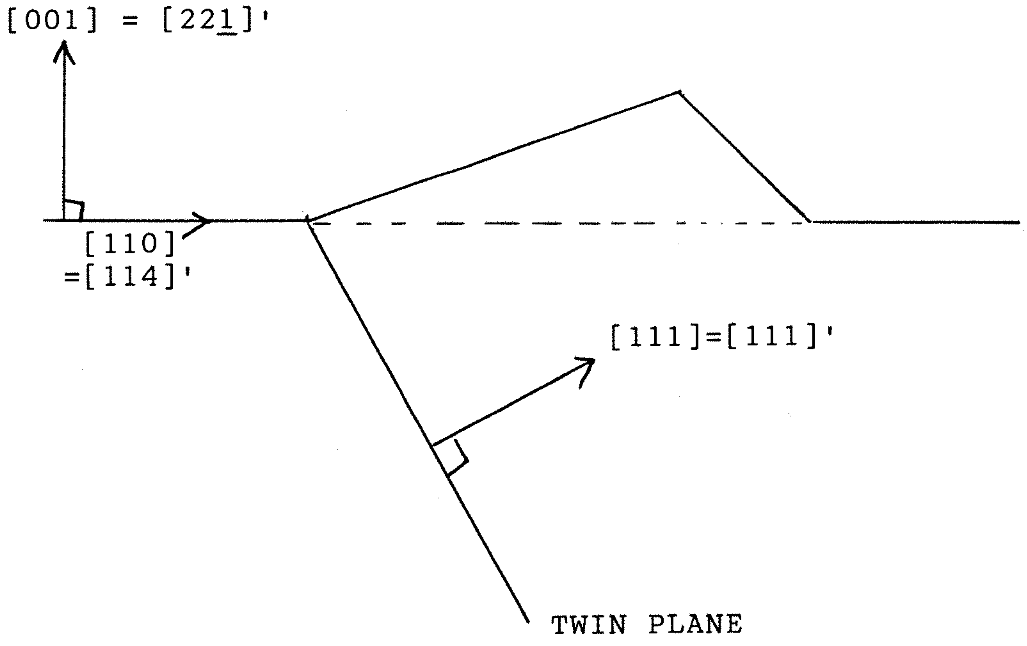

Figure 5.2: Theory proposed by the present author for the cross-section of a twinned hillock on (001) CMT.

On Figure 5.1, lines AB and AC are parallel to (010) and (100) respectively. Therefore, the plane which intersects (001) at AB lies in the (010) = $(2\underline{1}2)'$ zone. A low-order plane in this zone is $(10\underline{1})'$. Similarly, AC can be the intersection of $(01\underline{1})'$ with (001).

There are six distinct planes of the type (110)':

$(110)'$, $(1\underline{1}0)'$, $(101)'$, $(10\underline{1})'$, $(011)'$ and $(01\underline{1})'$.

If AB and AC are the intersection of planes of this type with (001), it is likely that other facets of the hillock are also of this type. $(1\underline{1}0)' = (\underline{1}10)$ which is normal to (001) and is not seen on the hillocks; (110)' is absent for the same reasons, which leaves (101)' and (011)'.

By calculation, (101)' = (141)
and (011)' = (411).

The intersections of these planes with (001) have the form (hk0) and by inspection are therefore $[4\underline{1}0]$ and $[1\underline{4}0]$ respectively. Both these directions make angles of 59.0^{o} with [110], which is consistent with their being planes on the hillock as shown in Figure 5.1.

The remainder of the faces are in the zone $[1\underline{1}0]$ by inspection, and are therefore of the form [hhl], e.g.:

(110)', (111)' etc.

Measurements of micrographs of hillocks in the present work are therefore consistent with the hypothesis that each hillock is a twin with low-order faces, predominately of the type (110)'.

5.1.3 Etch Techniques

Figure 4.4 shows a result of an etch in Polisar 2. Etching occured predominantly at the top edge of each hillock, suggesting either topological effects, or the presence of a lamellar defect in every hillock.

To test for the presence of topological effects, a fresh sample of this material was etched in a solution of Br_2 in methanol (1% by volume) until no sharp edges were visible on the hillocks. Then the samples were etched in Polisar 2. Figure 4.5 shows that the same defects are revealed. This result implies that each hillock surrounds lamellar defects in the CMT layer.

Figure 4.6 shows the results of an etch of Material A in the Polisar etch as modified by the present author. More linear features may be seen in this micrograph than in Figures 4.4 or 4.5. Some of these are associated with very faint features of the same shape as the hillocks but with reversed contrast - i.e., they are shallow, hillock-shaped depressions in the surface.

Figure 4.7 shows that all the features revealed by the modified Polisar etch on material 'A' persisted after etching with bromine/methanol. This was the case at all depths, except that they appeared smaller with increasing depth. The hillock-shaped features with reversed contrast appeared more prominently, and seemed slightly smaller than their raised counterparts. This result suggests that each hillock surrounds many lamellar defects which span the thickness of the layer, tapering towards the substrate.

5.1.4 White-Beam Synchrotron X-ray Topography

Figure 4.8 shows a reflection syncrotron X-ray topograph of the same material as Figures 4.1-7. The scale is such that the black spots could correspond to hillocks. The diffracting condition was such that twinned material would appear dark. However, other defects could also appear dark. The crescent-shaped features on the photograph, which correspond to depressions, suggest that the low angle of the incident radiation in this diffracting condition was causing topographical contrast. However, the wavy edge of the image from this straight sample suggests a degree of bend in the sample, so the contrast from the depressions could be due to lattice distortion. Also, the depressions show no darkened regions, which suggests that the contrast of the hillocks (dark) is unlikely to be of the same origin. More work is required here, but the ease with which features were observed under non-optimised conditions holds out hope for this technique.

5.2 The Effect of Precursors on CdTe Buffer Layers

Material 'B' (DIPT, lots of hillocks on the CMT) showed fine structure (Figures 4.12-4.13): elliptical features, distributed with no apparent order, of approximate dimensions 50x30x6nm.

Material 'C' (MATe, few hillocks on the CMT) showed a smooth, undulating, strongly oriented, almost faceted surface, with isloated valleys approximately 10x1um containing sharp discontinuities about 10nm across (Figures 4.14-4.15).

These results may be interpreted with reference to Section 2.3 of this work. MATe causes CdTe to have a surface more like that expected from F-vdM growth; DIPT causes more of an 'island growth' morphology.

According to theory, then, whatever is the adsorbed species when MATe is present diffuses faster that that when DIPT is present.

This suggests that the Cd and Hg surface mobilities are sufficiently high for the addition of Te to a growth step to be rate-determining.

Mar et al. (1984) suggested that the chemistry of the Te alkyl in this system controlled the orientation of growth; Bell et al. (1992) have investigated the cemistry of the decomposition of various organic tellurium compounds. Cinader (1991) proposed a model for growth controlled by one of the MOVPE precursor compounds.

5.3 The Topography of LPE CMT Layers

Material 'D' showed growth spirals on the terraces (Figures 4.16-4.17). The terrace spacing was about 2um. Spirals in both senses were observed. They were isotropic.

Both the reduced misfit in this system when compared with a CdTe buffer layer on GaAs, and the potentially different availability of growth species could effect this significantly different surface morphology. Indeed, each dislocation in this layer is represented by a growth spiral. These images were hard to locate, indicating that the dislocation density of this LPE material is very low at the surface.

5.4 Transmission Electron Microscopy

5.4.1 Materials 'B' and 'C' in Cross-Section

Materials 'B' and 'C' were CdTe buffer layers on 2^{o}-off (001) towards (011) GaAs. 'B' was produced using di-isopropyl tellurium, $((CH_3)_2CH)_2Te$. It was examined in cross-section by the route described above.

One feature expected of the sample was a series of dislocations at the CdTe:GaAs heterointerface, to accommodate the 14% misfit between the two compounds when relaxed. To observe this in atomic detail, the incident electron beam had to be aligned with a low-index direction in the sample by tilting the sample in the microscope. The samples were sectioned normal to the surface: so, with normal tilt, the plane of the sample would be parallel to the electron beam. As [001] is nearly normal to the sample surface, other low-index directions in the [001] zone should be expected in the plane of the sample. These would then be aligned with the electron beam by tilting the sample about the original surface normal. For technical simplicity, then, the first experiments were performed with the sample in a single-tilt holder, aligned to allow tilting about the original surface normal. This worked remarkably well, indicating that accurate alignment had been achieved at all stages of preparation. The only point in the preparation route where alignment by eye was required was in the sectioning of the sandwich rod: and this could be arranged to allow misorientation only about the original sample normal.

The nearest low-index direction to the sample normal was $(1\underline{1}0)$. Figure 4.18 is the electron diffraction pattern from a large region of the sample including both CdTe and GaAs. The major intensity maxima may easily be indexed, as in Figure 4.19: each is a doublet, the innermost of each pair being due to the CdTe (larger lattice parameter) and the outermost to GaAs (smaller lattice parameter). However, four obvious, slightly streaked peaks remain. Their spacing is consistent with their being associated with the CdTe. They can be indexed as either $(\frac{1}{2}\frac{1}{2}\frac{1}{2})$ or (0001) in the hexagonal system, both 'forbidden' maxima though only $(\frac{1}{2}\frac{1}{2}\frac{1}{2})$ is systematically forbidden.

Observation of the (111)-type doublets shows that they are not in line with the (000) intensity maximum. This suggests that the diffraction pattern is elongated towards (002) relative to that for CdTe. This is consistent with the lattice of CdTe being elongated towards [002] (the original layer normal) relative to that of GaAs. This is what would be observed if the CdTe was not fully relaxed. Basic measurement shows that the residual strain would have to be of the order of 2%.

The sample was then photographed in bright field (using only undiffracted radiation) with [110] electron beam. Figure 4.20 shows a dislocation network in the sample (the dark lines). The dislocation density is very high at the heterointerface (bottom of image).

Figure 4.21 shows a thinner region at a similar magnification to that of Figure 4.20. Lamellar features (suggested on Figure 4.20, with hindsight) appear clearly. These lie on (111) planes, if the heterointerface can be assumed to be close to (001). Most are seen on only one of the two possible sets of (111) planes. A few dislocations are seen which don't end at the heterointerface. Moiré fringes are seen at the heterointerface, showing regions where the incident beam passes through both CdTe and GaAs. This shows that the interface is not perfectly normal to (110). This might be either surface irregularity or evidence of the 2^{o} offset of the heterointerface from (001). Or, the existence of only one set of lamellar features when two are required by symmetry may be stronger evidence of this. Moiré fringes are also seen when the ion-beam thinning stage produces redeposition of GaAs over the CdTe by mistake (Figure 4.22).

Figure 4.23 is atomic resolution, taken with an aperture about the (111) and (000) diffracted beams, to reveal lattice fringes. This image shows that the lamellar features are twins, though their diffraction maxima cannot be seen on the diffractogram.

Figure 4.24 shows a region of the heterointerface, taken in atomic resolution with (000), (111) and $(11\underline{1})$ diffracted beams. It clearly illustrates the different lattice parameters of the CdTe and the GaAs, and indicates that dislocations exist at the heterointerface. It also suggests that a small misorientation exists between the two compounds.

Figure 4.25 is a low-magnification image, showing the full thickness of the buffer layer, and the distribution of the above features. Bend contours are clearly visible.

A similar examination of material 'C' (CdTe on 2^{o}-off (001) towards (110) GaAs using methyl allyl tellurium precursor, $CH_3TeCH_2CHCH_2$) was not possible in the time available for this work. This would seem to be essential in future work. Also, the link between the topography seen above and this TEM work remains obscure: for example, are valley features associated with lamellae in the bulk?

5.4.2 Material 'E' in Plan-view

Material 'E' was a complex heterostructure. Each section was examined in plan-view, as described above. The low-index direction nearest the sample normal was therefore (001), and all plan-view samples were therefore aligned with (001) as close as possible to the electron beam with a single-tilt holder. Atomic resolution was not desired as heterointerfaces were not expected in these samples.

The layers of the samples were:

n^+, high Cd
n^-, low Cd
p-type, high Cd
CdTe
GaAs, 2^{o}-off (001) to (110)

The n^+, high Cd region was examined at low magnification (Figure 4.26). This was in order to assess dislocation density at the surface. Through-plane (normal to the surface) dislocations appeared as short, stripy lines. There was probably some sample damage, however, appearing as streaks with many associated dislocations, which made any measurement of dislocation density potentially unreliable.

The n^-, low Cd region was very different. It contained a second phase, in the form of coherent, approximately circular lamellae. In Figure 4.27, with the incident electron beam parallel to [001], none appears edge on; in Figure 4.28, some of the lamellae appear nearly edge-on towards the bottom of the image, where the sample is bent. The angle between the two orientations exhibited by the lamellae in this region suggests that they are on (111) planes. The dark stripes across this image are bend contours.

The (100) diffraction pattern of this region is also unusual (Figure 4.29). It shows 'forbidden' (100) maxima as well as those expected, as indexed in Figure 4.30. If an aperture is placed around a (200) maximum in this diffraction pattern, some but not all the lamellae appear bright in the resulting dark-field image (Figure 4.31).

These features were again absent in the p-type, high Cd region of the sample (Figure 4.32). Threading dislocations (approximately normal to the plane of the sample) could be seen in abundance.

A low magnification image of the CdTe buffer layer of material 'E' in plan-view (Figure 4.33) showed many defects. This CdTe is prepared with the same precursor as that of material 'C', methyl allyl tellurium. Figure 4.34 shows a (110) diffraction pattern of this area. Short, smeared reflections appear in the image, in positions which correspond to one set of (111) rotation twins. The reflections are extended in the $[11\underline{1}]$ direction, and this indicates that the twins take the form of $(11\underline{1})$ lamellae. This suggests that the defects seen in Figure 4.33 are the lamellar twins seen in Figures 4.21 and 4.23. That only one set of twin reflections appears in Figure 4.34 shows that, in the chosen (110) projection, only one set of twins is dominant, as is suggested by Figure 4.21 and 4.23. This could be due to the 2° misorientation of the substrate. However, Figure 4.34 suggests that twins exist in both (110) projections, which could not be ascertained from Figures 4.21 and 4.23, and could not be predicted from the symmetry of the crystal structure, as discussed above.

5.4.3 Likely structure of Second Phase in Low-Cd CMT

The second phase clearly appeared as laminae on (111) planes.

The (001) diffraction pattern of the material showed faint (100) and (110) systematically absent reflections, suggesting the presence of a small volume fraction of superlattice; that is, material where the Cd and Hg atoms were ordered, giving rise to a larger primitive unit cell, a lower lattice point density, and a higher reciprocal lattice point density, with the potential for diffraction at angles forbidden in the unordered phase.

The lamellae showed no associated strain or dislocations and were therefore coherent with the matrix.

The (200) reflection is absent in diamond. The diamond structure is a special case of the sphalerite structure in which cationic and anionic sites are indistinguishable. All the atoms in diamond (an element) have equal structure factor. Thus the intensity of the (200) reflection in sphalerite is a function of the difference between the average structure factors of cationic and anionic sites. The observed contrast between lamellae and matrix in (200) dark-field TEM therefore indicates that the cationic and anionic structure factors of the lamellae and matrix are different. That is, the lamellae have a different composition to the matrix.

As this second phase was observed only in low-Cd material, these results may indicate that the reaction of the CMT to the specimen preparation route depends on the ratio of Cd to Hg. That is, the features may be artefacts. More work is required to confirm this, but their very existence remains a novel result.

5.4.4 The relaxation of a CdTe layer on GaAs

Twins were observed in a CdTe layer on GaAs, occurring as lamellae starting at the heterointerface and ending in the layer. They could be formed during stress relaxation, by one of two processes:

i. Expansion of partial dislocation loops from the interface

ii. Cooperative dissociation into partials of dislocations introduced from the surface.

The (111) planes crossing a twin were observed to deviate towards the plane of the interface. If these twins were formed by glide, they therefore caused expansion of the layer, which is consistent with an expansion of compressively strained CMT during relaxation.

According to theory, during the relaxation of a compressively strained layer, dislocations are introduced at the heterointerface whose extra half-planes are in the substrate. Either these are introduced from the surface, or dislocations of opposite sign are expelled from the interface.

The twins here end in dislocations whose extra half-planes run out of the free surface of the sample, not into the substrate. Therefore these dislocations would have moved towards free surface during relaxation.

If this structure were seen in a $(1\underline{1}0)$ projection of the structure instead of a (110) projection, all the dislocations would be of opposite type. This suggests that the relaxation structure could be different when viewed in $(1\underline{1}0)$ projection.

If relaxation occurs by the emission of dislocations from the heterointerface, the strain in the layer must be higher at the surface than at the heterointerface.

5.4.5 Diffraction pattern of CdTe on GaAs

The distortion of the diffraction pattern of CdTe suggests a strain of the order of 2% in the layer. Assuming relaxation occured by emission of dislocations from the heterointerface as discussed above, this observation can be accounted for if about one dislocation in seven of those required for complete (14%) relaxation is pinned near the heterointerface. Complete relaxation implies about one dislocation per seven lattice spacings, so a residual strain of 2% implies about one pinned dislocation per 50 lattice spacings, or one dislocation per 30nm. This seems a fair agreement with the structure observed experimentally.

No explanation is apparent for the observed $(\frac{1}{2}\frac{1}{2}\frac{1}{2})$ intensity maxima.

6. CONCLUSION & FUTURE WORK

6.1 Hillocks

Hillocks are crystalline.

They have an orientation relationship with the matrix.

They nucleate at the CdTe buffer layer.

Each could consist of a single twin with (110) faces, impling that (110) is the slowest growing face in this system.

Each hillock contains lamellar defects which pass through the entire layer, tapering towards the substrate.

6.2 Buffer Layers and Precursors

The addition of Te to a CdTe growth step is rate-determining.

Surface diffusion of growth species is faster in a MATe system that in a DIPT system. This affects the degree to which the growth is three-dimensional.

CdTe on GaAs relaxes by the expulsion of complete and partial dislocations from the heterointerface. About 1 in 7 of these becomes pinned near the interface, leaving a residual strain of about 2% in the layer. Many of the dislocations are partial and by their passage introduce twins into the CdTe. Very few of these twins penetrate the full thickness of the layer. Of the two possible symmetrically related sets of lamellar twins seen edge-on in (110) projection, one is dominant.

6.3 Second Phase in CMT

A previously unobserved coherent lamellar ordered phase has been observed on (111) planes in CMT with low Cd content.

Its composition is different to that of the matrix.

The phase may have been generated by the sample preparation route.

6.4 Future Work

CdTe buffer layers on GaAs substrates must be examined by TEM in all three perpendicular directions. The results must be interpreted in terms of layer growth conditions, the effects of substrate surface orientation, and the crystal symmetry.

A selective etch should be developed for buffer layers and cross-sections of layers. Ideally a very weak etch would be developed whose etch pits would be of a similar size to the features being etched, and which could be examined by AFM. In this way, any correlation between topographic and crystalline defects could be better explored.

Also, the relation between the topography of layers observed by AFM and their defect structure as observed by TEM should be explored in detail. This will involve the development of techniques to allow features to be correlated easily between the two techniques. This investigation will also require the observation of complete substrate-buffer-layer systems in cross-section, which in many ways is an aim in itself.

7. REFERENCES

Abdalla, M.I. & Holt, D.B.
Phys. Stat. Sol. 17 (1973) 267-279

Amirtharaj, P.M. & Pollak, F.H.
App. Phys. Lett. 45 (1984) 789-791

Amirtharaj, P.M., Tiong, K.K., Parayanthal, P., Pollak, F.H. & Furdyna, J.K.
J. Vac. Sci. Tech. A 3 (1985) 226-232

Angelo, J.E., Gerberich, W.W., Bratina, G., Sorba, L., Franciosi, A & Mills, M.J., in
Proceedings of the Materials Research Society 1993 Fall Meeting, Boston, Nov-Dec 1993,
Mat. Res. Soc. Symp. Proc. 319 (1994) 129-134,
Materials Research Society, Pittsburgh

Archer, N.A., Palfrey, H.D. & Willoughby, A.F.W.
J. Vac. Sci. Tech. A 3 (1985) 262-232

Archer, N.A., Palfrey, H.D. & Willoughby, A.F.W.
J. Cryst. Gr. 117 (1992) 177-182

Archer, N.A., Palfrey, H.D. & Willoughby, A.F.W.
J. El. Mats. 22 (1993) 967-971

Barbot, J.F., Rivaud, G. & Desoyer, J.C.
J. Mat. Sci. 23 (1988) 1655-1659

Barbot, J.F., Kronewitz, J. & Schroeter, W.
App. Phys. Lett. 57 (1990) 2689-2691

Bell, W., McQueen, A.E.D., Walton, J.C., Foster, D.F., Cole-Hamilton, D.J. & Hails, J.E.
J. Cr. Gr. 117 (1992) 58-66

Blomfield, C.J., Dharmadasa, I.M. & Gregory, G.E.
presented at the 1st International Conference on Materials for Microelectronics, Barcelona, October 1994

Bogoboyashchii, V.V., Elizarov, A.L., Ivanov-Omskii, V.I., Petrenko, V.R. & Petryakov, V.A.
Sov. Phys. Semicon. 19 (1985) 143-149

Brown, M. & Willoughby, A.F.W.
J. Phys. Coll. C6 (1979) 151-155

Brown, M. & Willoughby, A.F.W.
J. Vac. Sci. Tech. A 1 (1983) 1641-1645

Carlsson, L. & Ahlquist, C.N.
J. App. Phys. 43 (1972) 2529-2536

Cheng, T.T., Aindow, M., Jones, I.P., Hails, J.E., Williams, D.J. & Astles, M.G.
J. Cr. Gr. 135 (1994) 409-422

Cibert, J., Gobil, Y., Samindayar, K., Tatarenko, S., Chami, A., Feuillet, G., Dang, L.S. & Ligeon, E.
App. Phys. Lett. 54 (1989) 828-830

Chang, K.T. & Goo, E.
J. Vac. Sci. Tech. B 10 (1992) 1549-1552

Cinader, G., Raizman, A. & Sher, A.
J. Vac. Sci. Tech. B 9 1634-1638

Cinader, G. & Raizman, A.
J. App. Phys. 71 (1992) 2203-2205

Das, S.R., Rajan, K., van der Meer, P. & Cook, J.G.
Can. J. Phys. 65 (1987) 864-867

Faurie, J.P., Hsu, C., Sivananthan, S. & Chu, X.
Surf. Sci. 168 (1986) 473-482

Fewster, P.F., Cole, S., Willoughby, A.F.W. & Brown, M.
J. App. Phys. 52 (1981) 4586-4571

Frank, F.C. & van der Merwe, J.H.
Proc. R. Soc. A 198 (1949) 205-225

Garosshen, T.J., Kim, C.S. & Galligan, J.M.
J. El. Mats. 19 (1990) 889-894

Gasan-zade, S.G., Zhad'ko, I.P., Zinchenko, E.A., Romanov, V.A., Sal'kov, E.A. & Shepel'skii, G.A.
Sov. Phys. Semicon. 23 (1989) 52-55

Glass, H.L. & Appleby Woods, M.R.
App. Phys. Lett. 60 (1992) 2619-2621

Goesele, U., Frank, W. & Seeger, A.
App. Phys. 23 (1980) 361-368

Gorshkov, A.V., Zaitov, F.A., Shangin, S.B., Shalyapina, G.M., Petrov, I.N. & Asaturova, I.S.
Sov. Phys. Sol. State 26 (1984) 1787-1791

Holt, D.B. & Abdalla, M.I.
Phys. Stat. Sol. 26 (1974) 507-513

Iwanaga, H., Tomizuka, A. & Shoji, T.
J. Mat. Sci. Lett. 10 (1991) 975-977

Jones, C.L., Quelch, M.J.T., Capper, P. & Gosney, J.J.
J. App. Phys. 53 (1982) 9080-9092

Jones, C.L., Capper, P., Quelch, M.J.T. & Brown, M.
J. Cryst. Gr. 64 (1983) 417-432

Kirichenko, L.G. & Petrenko, V.F.
Sov. Phys. Sol. Stat. 22 (1980) 318-321

Klimakow, A. & Schenk, M.
Phys. Stat. Sol. A 115 (1989) K135-K137

Koestner, R.J. & Schaake, H.F.
J. Vac. Sci. Tech. A 6 (1988) 2834-2839

Koestner, R.J., Liu, H-Y., Schaake, H.F. & Hanlon, T.R.
J. Vac. Sci. Tech. A 7 (1989) 517-522

Koestner, R.J., Goodwin, M.W. & Schaake, H.F.
J. Vac. Sci. Tech. B 9 (1991) 1731-1737

Kraak, W., Kaldasch, J., Gille, P., Schurig, T. & Herrmann, R.
Phys. Stat. Sol. B 161 (1990) 613-627

Kröger, F.A.
'The Chemistry of Imperfect Crystals', vol. 2
2nd rev. ed., North-Holland Publishing Co., 1974

Kung, J-F., Behrensmeier, R. & Galligan, J.M.
Scripta Met. et Mat. 27 (1992) 1271-1276

Lastras-Martinez, A., Lee, U., Zhender, J. & Raccah, P.M.
J. Vac. Sci. Tech. 21 (1982) 157-160

Mar, H.A., Salansky, N. & Chee, K.T.
App. Phys. Lett. 44 (1984) 898-900

Marschall, J. & Milstein, F.
App. Phys. Lett. 62 (1993) 2784-2786

Matthews, J.W., Mader, S. & Light, T.B.
J. App. Phys. 41 (1970) 3800-3804

Matthews, J.W. & Blakeslee, A.E.
J. Cr. Gr. 27 (1974) 118-125

Million, A., DiCioccio, L., Gaillard, J.P. & Piaguet, J.
J. Vac. Sci. Tech. A 6 (1988) 2813-2821

Moore, T.M. & Schaake, H.F.
J. Vac. Sci. Tech. A 1 (1983) 1666-1668

Nakagawa, K., Maeda, K. & Takeuchi, S.
App. Phys. Lett. 34 (1979) 574-575

Nimtz, G., Schlicht, B. & Dornhaus, R.
App. Phys. Lett. 34 (1979) 490-491

Nouruzi-Khorasani, A., Jones, I.P., Dobson, P.S., Etem, Y., Williams, D.J., Astles, M.G., Ard, C. & Coates, G.
J. Cryst. Gr. 102 (1990) 819-826

Osip'yan, Y.A., Petrenko, V.F., Zaretskii, A.V. & Whitworth, R.W.
Adv. Phys. 35 (1986) 115-188

Otsuka, N., Kolodziejski, L.A., Gunshor, R.L., Datta, S., Bicknell, R.N. & Schetzina, J.F.
App. Phys. Lett. 46 (1985) 860-862

Pain, G.N.
J. Vac. Sci. Tech. B 10 (1992) 1485-1490

Pautrat, J.L., Magnea, N. & Faurie, J.P.
J. App. Phys. 53 (1982) 8668-8677

Pawlewicz, W.T., Allen, R.P., Barrus, H.G. & Lagreid, N.
Rev. Phys. App. 12 (1977) 417-422

Pellegrino, J. & Galligan, J.M.
Phys. Stat. Sol. A 110 (1988) 565-573

Pogrebnyak, V.A., Khalameida, D.D. & Yakovenko, V.M.
Sol. Stat. Comm. 65 (1988) 1307-1310

Ponce, F.A., Anderson, G.B. & Ballingall, J.M.
Surf. Sci. 168 (1986) 564-570

Raccah, P.M., Lee, U., Silberman, J.A., Spicer, W.E. & Wilson, J.A.
App. Phys. Lett. 42 (1983) 374-376

Saha, S., Pal, U., Samantaray, B.K., Chaudhuri, A.K. & Banerjee, H.D.
Thin Solid Films 164 (1988) 85-89

Schaake, H.F., Tregilgas, J.H., Lewis, A.J. & Everett, P.M.
J. Vac. Sci. Tech. A 1 (1983) 1625-1630

Schaake, H.F. & Tregilgas, J.H.
J. El. Mats. 12 (1983) 931-945

Schaake, H.F., Tregilgas, J.H., Beck, J.D. & Kinch, M.A.
Sol. Stat. Comm. 50 (1984) 133-136

Schaake, H.F., Tregilgas, J.H., Beck, J.D., Kinch, M.A. & Gnade, B.E.
J. Vac. Sci. Tech. A 3 (1985) 143-149

Scott, W. & Hager, R.
J. App. Phys. 42 (1971) 803

Speake, C.C., Smith, P.J., Lomer, T.R. & Whitworth, R.W.
Phil. Mag. A 38 (1978) 603-606

Spinulescu-Carnaru, I.
Phys. Stat. Sol. 15 (1966) 761-765

Sporken, R., Sivananthan, S., Reno, J. & Faurie, J.P.
J. Vac. Sci. Tech. B 6 (1988) 1204-1207

Talasek, R.T. & Syllaios, A.J.
J. Electrochem. Soc. 132 (1985) 656-659

Titchmarsh, J.M., Booker, G.R., Harding, W. & Wight, D.R.
J. Mat. Sci. 12 (1977) 341-346

Tobin, S., Smith, F.T.J., Norton, P.W., Wu, J., Dudley, M., DiMarzio, D. & Casagrande, L.G.
J. El. Mats. 24 (1995) 1189-1199

Tregilgas, J.H.
J. Vac. Sci. Tech. 21 (1982) 208-211

Tregilgas, J.H., Beck, J.D. & Gnade, B.
J. Vac. Sci. Tech. A 3 (1985) 150-152

Tregilgas, J.H., Polgreen, T.L. & Chen, M.C.
J. Cryst. Gr. 86 (1988) 460-466

van der Merwe, J.H.
J. El. Mats. 20 (1991) 793-803

Vydyanath, H.R.
J. Electrochem. Soc. 128 (1981) 2609-2629

Yoshikawa, M., Ueda, S., Maruyama, K. & Takigawa, H.
J. Vac. Sci. Tech. A 3 (1985) 153-155

Young, M.L. & Giess, J.
J. App. Phys. 69 (1991) 7173-7177

Zaitov, F.A., Stafeev, V.I., Khodakov, G.S.
Sov. Phys. Sol. Stat. 14 (1973) 2628-2629

Zaitov, F.A., Shalyapina, G.M., Shalyapina, L.M. & Mukhina, O.V.
Sov. Phys. Sol. Stat. 16 (1974) 774-775